Monthly Notices
of the
ROYAL ASTRONOMICAL SOCIETY

MNRAS **496,** 3668–3687 (2020)
Advance Access publication 2020 June 2

doi:10.1093/mnras/staa1496

# JINGLE – IV. Dust, H I gas, and metal scaling laws in the local Universe

I. De Looze,[1,2★†] I. Lamperti,[2] A. Saintonge,[2] M. Relaño,[3,4] M. W. L. Smith,[5] C. J. R. Clark,[6] C. D. Wilson,[7] M. Decleir,[6] A. P. Jones,[8] R. C. Kennicutt,[9,10] G. Accurso,[2] E. Brinks,[11] M. Bureau,[12,13] P. Cigan,[5] D. L. Clements,[14] P. De Vis,[5] L. Fanciullo,[15] Y. Gao,[16,17] W. K. Gear,[18] L. C. Ho,[19,20] H. S. Hwang,[21] M. J. Michałowski,[22] J. C. Lee,[21] C. Li,[23] L. Lin,[15] T. Liu,[24] M. Lomaeva,[2] H.-A. Pan,[15,25] M. Sargent,[26] T. Williams,[25] T. Xiao[15,27] and M. Zhu[28]

*Affiliations are listed at the end of the paper*

Accepted 2020 April 9. Received 2020 March 6; in original form 2020 January 10

**ABSTRACT**

Scaling laws of dust, H I gas, and metal mass with stellar mass, specific star formation rate, and metallicity are crucial to our understanding of the build-up of galaxies through their enrichment with metals and dust. In this work, we analyse how the dust and metal content varies with specific gas mass ($M_{\rm H\,I}/M_\star$) across a diverse sample of 423 nearby galaxies. The observed trends are interpreted with a set of Dust and Element evolUtion modelS (DEUS) – including stellar dust production, grain growth, and dust destruction – within a Bayesian framework to enable a rigorous search of the multidimensional parameter space. We find that these scaling laws for galaxies with $-1.0 \lesssim \log M_{\rm H\,I}/M_\star \lesssim 0$ can be reproduced using closed-box models with high fractions (37–89 per cent) of supernova dust surviving a reverse shock, relatively low grain growth efficiencies ($\epsilon = 30$–40), and long dust lifetimes (1–2 Gyr). The models have present-day dust masses with similar contributions from stellar sources (50–80 per cent) and grain growth (20–50 per cent). Over the entire lifetime of these galaxies, the contribution from stardust (>90 per cent) outweighs the fraction of dust grown in the interstellar medium (<10 per cent). Our results provide an alternative for the chemical evolution models that require extremely low supernova dust production efficiencies and short grain growth time-scales to reproduce local scaling laws, and could help solving the conundrum on whether or not grains can grow efficiently in the interstellar medium.

**Key words:** ISM: abundances – ISM: dust, extinction – galaxies: evolution – galaxies: star formation.

## 1 INTRODUCTION

Dust grains make up only a small fraction (∼1 per cent on average) of the interstellar mass in galaxies. None the less, these dust particles play a crucial role in balancing local gas heating and cooling processes. Chemical reactions on the surfaces of dust grains result in the formation of a large variety of molecules, especially in regions of the interstellar medium (ISM) where gas-phase chemistry is inefficient. The processing of about 30–50 per cent of all stellar light in the Universe by dust grains (e.g. Driver et al. 2007; Bianchi et al. 2018) makes observations of the infrared (IR) dust emission furthermore essential for all studies of star formation to recover the bright ultraviolet (UV) and optical light emitted by young stellar populations.

Although the ubiquitous presence of interstellar gas (Hartmann 1904) and dust (Trumpler 1930) has been recognized for nearly a century, the origin and main formation channels for interstellar dust grains remain an open question. It is commonly accepted that dust grains can form through the condensation of metals in the cool envelopes of asymptotic giant branch (AGB) stars (e.g. Ferrarotti & Gail 2006; Nanni et al. 2013) and in the expanding ejecta of core-collapse supernovae (e.g. Barlow et al. 2010; Gomez et al. 2012; Matsuura et al. 2015; De Looze et al. 2017a, 2019; Temim et al. 2017; Cigan et al. 2019), but these two stellar dust production sources appear not able to account for the bulk of the dust mass observed in galaxies at high redshifts (Michałowski et al. 2010;

---

★ E-mail: ilse.delooze@ugent.be, idelooze@star.ucl.ac.uk
† Institutional affiliations are shown at the end of the paper.

© 2020 The Author(s)
Published by Oxford University Press on behalf of the Royal Astronomical Society

Downloaded from https://academic.oup.com/mnras/article/496/3/3668/5850384 by University College London user on 24 September 2020

Valiante et al. 2011; Rowlands et al. 2014; Mancini et al. 2015; Michałowski 2015; Graziani et al. 2019) and in the nearby Universe (Matsuura, Woods & Owen 2013; De Looze et al. 2016; Schneider, Hunt & Valiante 2016; Ginolfi et al. 2018; Triani et al. 2020). The reformation of dust grains through the accretion of metals in dense ISM clouds is thought to provide the key to explaining the large amounts of interstellar dust observed in galaxies (e.g. Rowlands et al. 2014; Zhukovska 2014; Schneider et al. 2016; Zhukovska et al. 2016; De Vis et al. 2017b; Popping, Somerville & Galametz 2017), but the exact physical processes that enable this type of 'grain growth' in the ISM remain poorly understood (Barlow 1978; Ferrara, Viti & Ceccarelli 2016; Ceccarelli et al. 2018).

To better understand the main dust formation mechanisms in galaxies, and whether or not grain growth can dominate the dust production, we require substantial progress on two independent fronts. First of all, we need reliable estimates of the dust content in galaxies. In this work, we rely on a set of carefully determined dust masses (see Appendix A) inferred from fitting the mid-IR to submillimetre dust spectral energy distribution (SED) with a Bayesian method that builds upon the grain mix and dust properties from the THEMIS (The Heterogeneous dust Evolution Model for Interstellar Solids) dust model (Jones et al. 2017) and a multicomponent interstellar radiation field heating these dust grains (Dale et al. 2001). Secondly, we require measurements of how the dust, metal, and gas content in galaxies scales with respect to other global galaxy properties [i.e. stellar mass, specific star formation rate (sSFR), and metallicity] through scaling relations to infer how a galaxy's dust content evolves with time and to shed light on the main sources of dust production in the ISM. Understanding how the amount of dust, metals, and gas evolves for a large ensemble of galaxies, at different stages of their evolution, will allow us to pin down the importance of various dust production and destruction mechanisms. Tracking how metals and dust are built up throughout a galaxy's lifetime necessitates simultaneously quantifying dust and gas reservoirs. The JINGLE (JCMT dust and gas In Nearby Galaxies Legacy Exploration) galaxy sample (Saintonge et al. 2018, hereafter JINGLE Paper I) was designed to acquire dust mass measurements from the *Herschel* and SCUBA-2 data, in addition to ancillary H I observations, and molecular gas mass measurements currently available for 63 JINGLE galaxies.

In this paper, we present dust, gas, and metal scaling relations for a sample of 423 nearby galaxies, including JINGLE, HRS, HAPLESS, HiGH, and KINGFISH samples.[1] We split up this local galaxy sample into six subsamples according to their stage of evolution. We assume in this paper that the evolutionary stage of a galaxy is relatively well approximated by their $M_{\rm H\,I}/M_\star$ ratios and infer representative star formation histories (SFHs) according to the evolutionary stage of these galaxies. We compare the average dust, gas, and metal mass fractions along these evolutionary sequences with a set of Dust and Element evolUtion modelS (DEUS) in a Bayesian framework in order to cover a large range of input parameters and to elucidate what processes drive these scaling laws. This is the first study (to our knowledge) where such a rigorous search of the full parameter space has been pursued.

Section 2 discusses the main characteristics of our five nearby galaxy samples (JINGLE, HRS, KINGFISH, HAPLESS, and HIGH). In Section 3, we analyse the observed scaling laws for the dust, gas, and metal content of these five galaxy samples. In Section 4, we subdivide our local galaxy sample into six bins according to their specific H I gas masses, and compare their average scaling laws with DEUS to infer how their dust and metal content has been built up across cosmic time. In Section 5, we summarize our conclusions. In the appendices, we outline the method used to model the dust masses (Appendix A), detail the data sets and methods used to infer galaxy specific properties (Appendix B), describe how we infer customized SFHs for galaxies at different evolutionary stages (Appendix C), and discuss the specifics of DEUS (Appendix D), while a list of acronyms (see Table F1) and symbols (see Table F2) is presented in Appendix F, and additional tables and figures are presented in Appendices E and G.

## 2 SAMPLE DESCRIPTION

### 2.1 An introduction to JINGLE

JINGLE is a large programme on the James Clerk Maxwell Telescope (JCMT) aiming to assemble dust mass measurements for a sample of 193 local galaxies and molecular gas masses for part of this sample. The JINGLE sample populates the redshift range between $z = 0.01$ and 0.05, and was drawn from the MaNGA (Mapping Nearby Galaxies at Apache Point Observatory; Bundy et al. 2015) sample with optical integral-field spectroscopy data. In brief, JINGLE galaxies were selected to homogeneously sample the SFR–$M_\star$ plane between $10^9$ and $10^{11}$ $\mathrm{M}_\odot$. As part of the sample selection procedure, JINGLE galaxies were required to have detections in the *Herschel* SPIRE 250 and 350 μm bands. New JCMT SCUBA-2 850 μm (and 450 μm) observations probe the dust emission spectrum along the Rayleigh–Jeans tail (Smith et al. 2019, hereafter JINGLE Paper II), while RxA CO $J = 2$–1 observations provide measurements of the molecular gas content (currently) for 63 JINGLE galaxies (Xiao et al. in preparation, hereafter JINGLE Paper III). As a consequence of the sample selection, most JINGLE galaxies are classified as late-type spirals or irregular galaxies with a subset of only seven early-type galaxies.

The sample selection and main science goals of the JINGLE survey are described in JINGLE Paper I, with specific details about the observational set-up and data reduction of the RxA CO $J = 2$–1 line spectroscopy and SCUBA-2 450 and 850 μm dust continuum observations presented in JINGLE Papers III and II, respectively. In Lamperti et al. (2019) (hereafter JINGLE Paper V), a hierarchical Bayesian fitting algorithm has been used to infer dust temperatures, dust emissivity indices, and dust masses for the ensemble of JINGLE (and HRS) galaxies. In this paper, we rely on the dust masses for JINGLE and the other nearby galaxies inferred from an alternative modelling method using a non-hierarchical Bayesian implementation of the THEMIS dust model, which enables us to constrain the small grain size distribution, dust masses, and starlight intensity distribution responsible for the dust heating (see Appendix A). We note that the dust masses inferred here and in JINGLE Paper V are in excellent agreement after considering the differences in the assumed dust mass absorption coefficients: JINGLE Paper V assumes $\kappa_{500} = 0.051$ $\mathrm{m^2\,kg^{-1}}$ (Clark et al. 2016), while here we adopt $\kappa_{500} = 0.185$ $\mathrm{m^2\,kg^{-1}}$ from the THEMIS dust model (Jones et al. 2013, 2017). Due to growing evidence (from both observations and laboratory experiments) indicating that interstellar dust is more emissive than considered in the previous generation of dust models (e.g. Planck Collaboration XXIX 2016; Demyk et al. 2017a, b; Clark et al. 2019), we base our analysis upon the

---

[1] The combined galaxy sample consists of 568 galaxies. We consider the subsample of those galaxies: (1) with available H I gas measurements and (2) classified as non-H I-deficient galaxies.

Downloaded from https://academic.oup.com/mnras/article/496/3/3668/5850384 by University College London user on 24 September 2020

**Table 1.** Overview of the median values for a set of galaxy properties, with the error bars reflecting the dispersion observed for galaxies within a specific galaxy sample. For the HRS sample, we report the sample characteristics for the entire set of HRS galaxies, and the subsamples of H I-deficient and non-deficient (H $\text{I}_{\rm def} \leq 0.5$) HRS galaxies.

| Quantity | JINGLE | HRS (all) | HRS (H $\text{I}_{\rm def} < 0.5$) | HRS (H $\text{I}_{\rm def} \geq 0.5$) | KINGFISH | HAPLESS | HIGH |
|---|---|---|---|---|---|---|---|
| $12 + \log(\mathrm{O/H})$ | 8.74 ± 0.10 | 8.58 ± 0.15 | 8.57 ± 0.15 | 8.64 ± 0.13 | 8.69 ± 0.22 | 8.44 ± 0.17 | 8.50 ± 0.20 |
| $\log M_\star$ ($\mathrm{M}_\odot$) | 10.13 ± 0.55 | 9.67 ± 0.63 | 9.53 ± 0.59 | 9.95 ± 0.64 | 9.95 ± 0.98 | 9.06 ± 0.64 | 9.39 ± 0.86 |
| log SFR ($\mathrm{M}_\odot\ \mathrm{yr}^{-1}$) | 0.052 ± 0.48 | − 0.70 ± 0.67 | − 0.47 ± 0.56 | − 1.18 ± 0.65 | − 0.48 ± 0.85 | − 0.83 ± 0.31 | − 0.24 ± 0.54 |
| log sSFR ($\mathrm{yr}^{-1}$) | − 10.03 ± 0.49 | − 10.30 ± 0.80 | − 10.08 ± 0.51 | − 10.98 ± 0.82 | − 10.0 ± 0.63 | − 9.92 ± 0.68 | − 9.72 ± 0.50 |
| $\log M_{\rm H\,I}$ ($\mathrm{M}_\odot$) | 9.66 ± 0.39 | 8.92 ± 0.60 | 9.20 ± 0.44 | 8.37 ± 0.45 | 9.08 ± 0.71 | 8.90 ± 0.52 | 9.74 ± 0.48 |
| $D$ (Mpc) | 123.4 ± 41.6 | 17.0 ± 1.2 | 17.3 ± 2.8 | 17.0 ± 2.4 | 9.8 ± 6.8 | 31.1 ± 5.3 | 32.4 ± 5.0 |
| $\log M_{\rm dust}/M_\star$ | − 2.71 ± 0.36 | − 2.90 ± 0.43 | − 2.76 ± 0.29 | − 3.19 ± 0.55 | − 2.86 ± 0.48 | − 2.82 ± 0.46 | − 2.78 ± 0.44 |
| $\log M_{\rm H\,I}/M_\star$ | − 0.43 ± 0.48 | − 0.76 ± 0.75 | − 0.50 ± 0.50 | − 1.49 ± 0.66 | **− 0.60 ± 0.91** | − 0.35 ± 0.69 | 0.02 ± 0.61 |
| $\log M_{\rm dust}/M_{\rm metals}$ | − 0.67 ± 0.23 | − 0.60 ± 0.21 | − 0.62 ± 0.21 | − 0.44 ± 0.08 | − 0.63 ± 0.38 | − 0.65 ± 0.15 | − 0.78 ± 0.30 |
| $\log M_{\rm dust}/M_{\rm H\,I}$ | − 2.25 ± 0.31 | − 2.17 ± 0.47 | − 2.28 ± 0.35 | − 1.80 ± 0.44 | − 2.30 ± 0.69 | − 2.59 ± 0.23 | − 2.61 ± 0.45 |

dust masses inferred with the THEMIS dust model to account for this increased dust emissivity and to avoid overestimating the dust masses for a set of observed flux densities (compared to the previous generation of dust models).

### 2.2 Nearby galaxy comparison samples

In addition to JINGLE, we have selected four nearby galaxy samples with well-studied dust characteristics and general galaxy properties. The combination of samples, while not statistical, allows the scaling relations in this paper to be explored over the widest possible extent of the parameter spaces in question.

The first sample consists of the galaxies from the *Herschel* Reference Survey (HRS; Boselli et al. 2010), which is a volume-limited, *K*-band-selected sample of 322 nearby galaxies with distances between 15 and 25 Mpc. More than half of the HRS sample consists of cluster galaxies (residing in the Virgo and Ursa Major cluster), with the remaining galaxies located in massive groups surrounding these clusters. The second sample is composed of galaxies from the *Herschel* programme KINGFISH (Key Insights on Nearby Galaxies: A Far-Infrared Survey with *Herschel*; Kennicutt et al. 2011) that consists of 61 nearby galaxies with distances $D \leq 30$ Mpc, covering a variety of different morphological classifications, star formation activity, and galaxy environments. The third and fourth samples, HAPLESS and HiGH, were selected from the *Herschel* Astrophysical Terahertz Large Area Survey (H-ATLAS; Eales et al. 2010) based on their SPIRE 250 μm (HAPLESS; Clark et al. 2015) and H I (HiGH; De Vis et al. 2017a) detections, respectively. Since dusty galaxies often contain a considerable amount of gas and vice versa, it is not surprising that the HAPLESS (42 galaxies) and HiGH (40 galaxies) samples have 22 sources in common. Average sample properties are summarized in Table 1, and are briefly discussed in Section 2.3. To compare properties of different galaxy samples, we have performed Mann–Whitney U-tests using the `RS_TEST` procedure in IDL (see Table E1 for the test results). This procedure tests the hypothesis that two samples have the same median of distribution at a significance level of 5 per cent, with probabilities higher than this value indicative of both samples not being significantly different.

### 2.3 Sample characteristics

JINGLE and KINGFISH galaxies are more metal rich as compared to other nearby galaxy samples (see Fig. 1a), whereas the oxygen abundance distributions for HRS, HAPLESS, and HiGH samples are not considered to be significantly different. The JINGLE sample has a relatively flat stellar mass distribution (which was by selection; see JINGLE Paper I) with values ranging from $10^9$ to $10^{11}$ $\mathrm{M}_\odot$ (see Fig. 1b), significantly different from the other four nearby galaxy samples. The HRS, KINGFISH, and HiGH samples extend towards low stellar masses with several galaxies in the $10^6$–$10^9$ $\mathrm{M}_\odot$ stellar mass range. HAPLESS does not contain galaxies with stellar masses below $10^8$ $\mathrm{M}_\odot$, nor does it contain many $M_\star > 10^{10}$ $\mathrm{M}_\odot$ galaxies like JINGLE. Based on the mass–metallicity relation (e.g. Tremonti et al. 2004; Hughes et al. 2013; Sánchez et al. 2017), it is thus not surprising that JINGLE galaxies are characterized by the highest metal abundances among our local galaxy sample.

The median SFR of JINGLE galaxies (1 $\mathrm{M}_\odot\ \mathrm{yr}^{-1}$; see Fig. 1c) is similar to the average present-day star formation activity in our own Galaxy (Robitaille & Whitney 2010). SFRs are a factor of 3 lower in KINGFISH and HiGH galaxies, and lower by a factor of 6 in HRS and HAPLESS galaxies, than those for JINGLE galaxies. The low SFRs and sSFRs imply that the majority of HRS galaxies are undergoing a period of low star formation activity, and have built up the majority of their stellar mass content during earlier epochs. The subsample of more evolved HRS galaxies is also evident from the long tail in the sSFR diagram at the low-sSFR end (see Fig. 1d). Although HiGH, KINGFISH, and HAPLESS galaxies have a median SFR two, three, and eight times lower than JINGLE, respectively, the similarity in their median sSFRs suggests that these samples contain several galaxies with elevated levels of recent star formation activity.

The H I mass content of JINGLE galaxies is similar to the median H I reservoirs present in the H I-selected HiGH sample, but the specific H I gas mass of HiGH galaxies ($\log M_{\rm H\,I}/M_\star = 0.02 \pm 0.61$) is higher than that for JINGLE ($\log M_{\rm H\,I}/M_\star = -0.43 \pm 0.48$). HiGH galaxies are therefore considered to be in a very early stage of galaxy evolution (De Vis et al. 2017a). None the less, JINGLE H I masses are clearly higher than those of KINGFISH, HAPLESS, and HRS galaxies, suggesting that JINGLE galaxies have retained a non-negligible part of their H I reservoir for future star formation, and are also at an earlier stage of galaxy evolution. It is worth noting that the spatial extent of the H I reservoir has not been taken into consideration in the comparison of these H I masses (due to the availability of single-dish measurements only), and that, in particular, low-mass metal-poor galaxies can have a large H I reservoir that extends well beyond the stellar body (e.g. Hunter et al. 2011). HRS galaxies have a median H I mass almost an order of magnitude below the median for JINGLE, which supports

Downloaded from https://academic.oup.com/mnras/article/496/3/3668/5850384 by University College London user on 24 September 2020

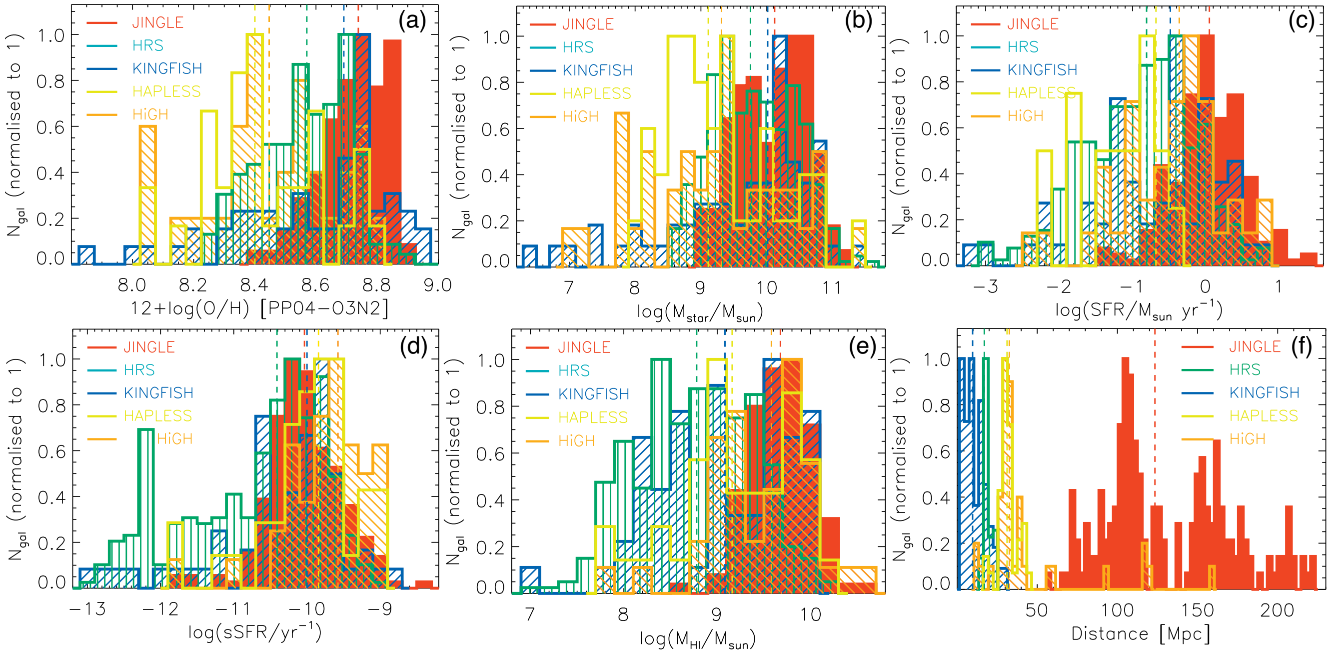

**Figure 1.** From left to right and top to bottom: histograms of the metallicities (as traced by the oxygen abundance), stellar masses, SFRs, sSFRs, H I masses ($M_{\rm H\,I}$), and distances for the JINGLE (red filled histograms), HRS (green vertical lines), KINGFISH (blue diagonal lines), HAPLESS (yellow lines), and HiGH (orange diagonal lines) galaxies. Median sample values are indicated with vertical dashed lines using the same colour coding.

the interpretation of the HRS sample consisting of more evolved galaxies. A subset of the HRS galaxies has been characterized to be H I deficient,[2] and their reduced star formation activity has been attributed to the removal of part of their H I gas reservoir due to environmental processes that inhibit new stars from forming (e.g. Cortese et al. 2011).

The median distance of JINGLE galaxies ($D$ = 123.4 Mpc) is higher than the median distances ($D$ = 10–30 Mpc) for the other samples, which will likely bias the JINGLE sample selection to only include the dustiest galaxies at those distances.

Similar to the low fraction of early-type galaxies in the JINGLE sample (i.e. 3.6 per cent), the HAPLESS and HiGH samples consist of late-type star-forming galaxies with a range of different morphologies (ranging from early-type spirals to bulgeless highly flocculent galaxies), with the exception of two early-type HAPLESS galaxies. The KINGFISH sample contains 10 early-type galaxies (E/S0/S0a), 22 early-type spirals (Sa/Sb/Sbc), 16 late-type spirals (Sc/Sd/Scd), and 13 irregular galaxies (I/Sm). The HRS sample contains a significant subpopulation of 23 elliptical and 39 spheroidal galaxies (Smith et al. 2012), with the remaining 261 galaxies classified as late-type galaxies.

## 3 DUST, GAS, AND METAL SCALING LAWS

The main goal of this part of the paper is to analyse local dust, H I gas, and metal scaling laws, to understand how the dust content and metallicity evolve over time, and what processes drive this evolution.

### 3.1 Dust scaling relations

With dust being formed through the condensation of metals synthesized in recent generations of stars, the dust content is closely linked to the stellar mass and star formation activity in galaxies. Since the stellar mass typically scales with the metal richness of the ISM (through the stellar mass–metallicity relation; e.g. Tremonti et al. 2004), the dust-to-stellar mass ratio can be interpreted as the ratio of metals locked into dust grains versus the metals in the gas phase. It is known that specific dust masses ($M_{\rm dust}/M_\star$) decrease towards high stellar masses (see Fig. 2, left-hand panel) due to dust destruction dominating over dust production processes in more massive systems. The latter trend can also be understood in view of the downsizing of galaxies (e.g. Cowie et al. 1996), where most of the massive galaxies already converted most of their gas into stars, and the bulk of dust mass was formed during these main star formation episodes. The wide spread in log $M_{\rm dust}/M_\star$ ratio from −2.5 to −5 that we find for galaxies with stellar masses $M_\star = 10^{10}–10^{11}\,{\rm M}_\odot$ is a reflection of galaxies with similar stellar masses but at different stages of evolution.

JINGLE galaxies populate the high end of the $M_{\rm dust}/M_\star$ range at a given stellar mass. Their high log $M_{\rm dust}/M_\star$ ratios ($-2.71 \pm 0.36$) are not surprising considering that JINGLE galaxies were selected from their detections in the *Herschel* SPIRE bands (JINGLE Paper I). The JINGLE galaxies have $M_{\rm dust}/M_\star$ ratios similar to (or even slightly higher than) the majority of dust- and H I-selected HAPLESS/HiGH galaxies in the stellar mass range that those samples have in common. Several KINGFISH and HAPLESS/HiGH galaxies with stellar masses $M_\star \leq 10^9\,{\rm M}_\odot$ are characterized by low $M_{\rm dust}/M_\star$ ratios, and deviate from the general trend for more massive galaxies. The HAPLESS/HiGH galaxies with low specific dust masses were identified by De Vis et al. (2017a) as a unique population of galaxies, at an extremely early phase of evolution where most of the dust still needs to be formed. H I-deficient HRS

---

[2] The H I deficiency is calculated as the logarithmic difference between the expected and observed H I mass, i.e. H I def $= \log M_{\rm H\,I,ref} - \log M_{\rm H\,I,obs}$, following the definition in Haynes & Giovanelli (1984).

Downloaded from https://academic.oup.com/mnras/article/496/3/3668/5850384 by University College London user on 24 September 2020

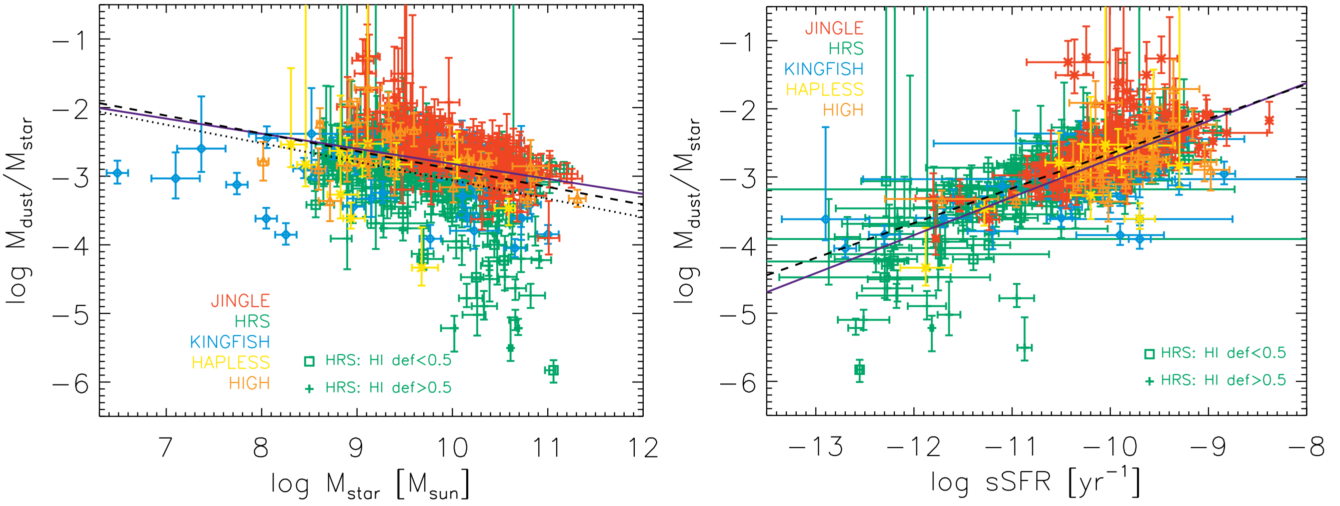

**Figure 2.** The scaling of the dust-to-stellar mass ratio (i.e. $M_{\rm dust}/M_{\star}$) with stellar mass ($M_{\star}$, left-hand panel) and specific star formation rate (sSFR with sSFR = SFR/$M_{\star}$, right-hand panel) is shown for JINGLE (red cross), HRS (green square/cross), KINGFISH (blue diamond), HAPLESS (yellow cross), and HiGH (orange triangle) galaxies. A distinction is made between H I-deficient and non-deficient HRS galaxies ($\mathrm{H\,I}_{\rm def} \leq 0.5$, green square). Best-fitting relations (as inferred for the entire nearby galaxy sample, with the exception of H I- deficient HRS galaxies) have been overlaid as a purple solid line, and are compared (where possible) to local galaxy scaling laws from De Vis et al. (2017a) (black dashed curve) and from Casasola et al. (2019) (black dotted curve). The scaling relation from De Vis et al. (2017a) was adjusted to account for the difference in the assumed dust opacities.

galaxies populate the bottom part of the diagram with systematically lower $M_{\rm dust}/M_{\star}$ ratios in comparison to other nearby galaxies. The lower $M_{\rm dust}/M_{\star}$ for H I-deficient galaxies suggests that these galaxies have had part of their dust content stripped along with their H I gas content (see also Cortese et al. 2014), or that star formation has ceased in these objects a long time ago, resulting in a lack of recent dust replenishment, with dust destruction processes further diminishing their dust content. Our best-fitting relation is very similar compared to the best-fitting relation from De Vis et al. (2017a) (inferred for HRS, HAPLESS, and HiGH late-type galaxies). The relation inferred by Casasola et al. (2019) for a sample of 436 late-type local DustPedia galaxies is lower by up to 0.2 dex, which can likely be attributed to a selection effect. Our sample includes dust-selected galaxies at larger distances (see Fig. 1f), which are likely to be dustier on average compared to a local galaxy sample.

The importance of recent star formation activity to determine a galaxy's dust content is evidently shown from the scaling of $M_{\rm dust}/M_{\star}$ with sSFR (see Fig. 2, right-hand panel). Independent of their morphological classification, all galaxies follow a similar trend of decreasing $M_{\rm dust}/M_{\star}$ towards low sSFR over three orders of magnitude in both quantities. The tight correlation ($\rho = 0.63$) between $M_{\rm dust}/M_{\star}$ and sSFR was first shown by da Cunha et al. (2010) for a sample of nearby galaxies. The fact that dust-selected samples such as JINGLE and HAPLESS follow the same trend as the stellar mass-selected HRS sample indicates that sSFR is a more fundamental parameter than $M_{\star}$ to determine the specific dust mass of a galaxy (either directly or through a secondary correlation).

The present-day dust mass of a galaxy is set by the balance between the sources producing dust (i.e. evolved stars, supernovae, grain growth) and the sinks destroying dust grains (i.e. astration, supernova shocks). The observed correlation between $M_{\rm dust}/M_{\star}$ and sSFR could be a reflection of an equilibrium process where the amount of dust grains formed/destroyed scales with the recent star formation activity in a galaxy. Alternatively, the relation of the $M_{\rm dust}/M_{\star}$ with sSFR can be interpreted as an indirect measure of the total gas mass in a galaxy that is known to scale with the SFR through the Kennicutt–Schmidt relation (Schmidt 1959; Kennicutt 1998). Given that the $M_{\rm H\,I}/M_{\star}$ ratio dominates the scatter in local scaling relations with $M_{\star}$ and sSFR (see also Section 3.2), and correlates strongly with the observed $M_{\rm dust}/M_{\star}$, $M_{\rm dust}/M_{\rm metals}$, and $M_{\rm dust}/M_{\rm HI}$ ratios in our local galaxy samples, we favour the latter interpretation (see below).

### 3.2 H I gas scaling relations

With dust grains making up about 1 per cent of the ISM in mass, the gas reservoir dominates the ISM budget of a galaxy. In this paper, we will make the assumption that galaxies with massive H I reservoirs (compared to their $M_{\star}$) are considered to be at an early stage of evolution, while a low gas content is indicative of an evolved galaxy that had most of its gas reservoir turned into stars already. The $M_{\rm H\,I}/M_{\star}$ ratio in Fig. 3 (left-hand panel) shows a similar anticorrelation ($\rho = -0.64$) with stellar mass as the $M_{\rm dust}/M_{\star}$ ratio in Fig. 2 (left-hand panel) that is consistent with the least massive galaxies having the largest atomic gas reservoir proportional to their stellar mass.

Our best-fitting relation for the specific H I gas mass as a function of stellar mass is shifted upwards by 0.3–0.4 dex compared to the trend from De Vis et al. (2017a) due to the high specific H I gas masses of JINGLE galaxies, and due to our omission of H I-deficient HRS galaxies to determine the best-fitting relation. The scatter observed in the relations of $M_{\rm H\,I}/M_{\star}$ with $M_{\star}$ ($\sigma = 0.57$) and sSFR ($\sigma = 0.40$) dominates over the dispersion in the respective trends of $M_{\rm dust}/M_{\star}$ with $M_{\star}$ ($\sigma = 0.39$) and sSFR ($\sigma = 0.29$), which suggests that the scatter in the trends of $M_{\rm dust}/M_{\star}$ with $M_{\star}$ and sSFR are likely dominated by variations in the galaxy's specific H I gas masses, and not necessarily directly influenced by the various dust production and destruction mechanisms at work in these galaxies. This scenario is also supported by the scatter observed in the scaling laws (see Fig. 4) for $M_{\rm dust}/M_{\rm H\,I}$ with $M_{\star}$ ($\sigma = 0.33$) and sSFR ($\sigma = 0.37$), which is lower than similar relations for $M_{\rm H\,I}/M_{\star}$ and suggests that the specific H I gas mass dominates the scatter in these scaling

Downloaded from https://academic.oup.com/mnras/article/496/3/3668/5850384 by University College London user on 24 September 2020

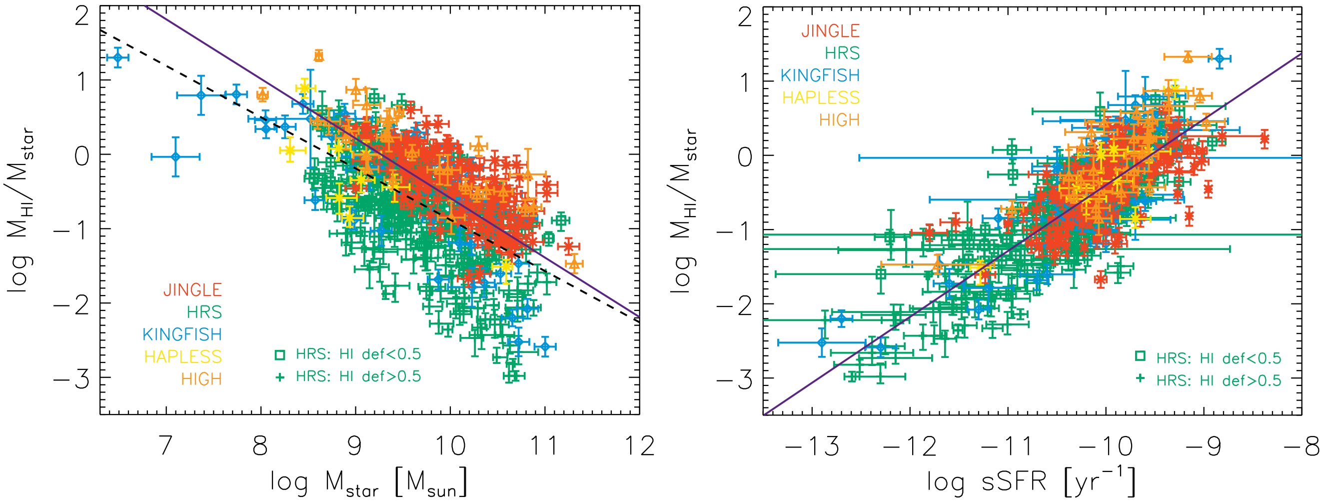

**Figure 3.** The scaling of the H I-to-stellar mass ratio (i.e. $M_{\rm H\,I}/M_\star$) with stellar mass ($M_\star$, left-hand panel) and specific star formation rate (sSFR with sSFR = SFR/$M_\star$, right-hand panel). See the caption of Fig. 2 for more details on the symbols and plotted curves.

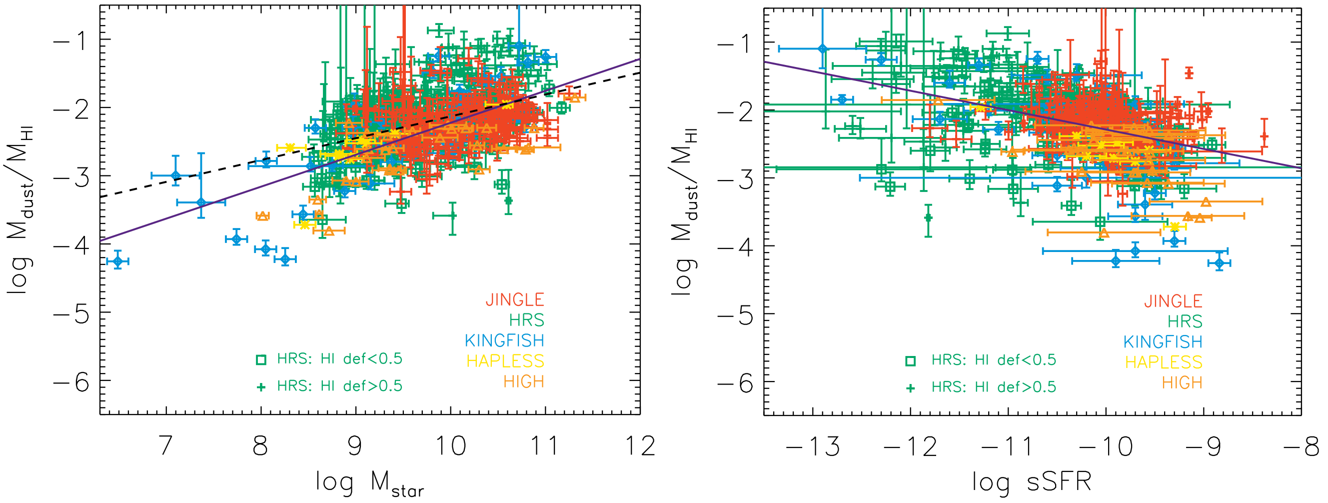

**Figure 4.** The scaling of the dust-to-H I mass ratio (i.e. $M_{\rm dust}/M_{\rm H\,I}$) with stellar mass ($M_\star$, left-hand panel) and specific star formation rate (sSFR with sSFR = SFR/$M_\star$, right-hand panel). See the caption of Fig. 2 for more details on the symbols and plotted curves.

relations. The trends between $M_{\rm H\,I}/M_\star$, and $M_{\rm dust}/M_\star$ ($\rho = 0.67$), $M_{\rm dust}/M_{\rm metals}$ ($\rho = -0.61$), and $M_{\rm dust}/M_{\rm H\,I}$ ($\rho = -0.72$) furthermore show strong correlations (see Fig. 8 and Table 2) compared to the relations of the latter ratios with $M_\star$ or sSFR, reinforcing the above reasoning. To study what processes drive the observed trends and scatter in local scaling laws, we therefore verify how the dust and metal content of these galaxies varies as a function of $M_{\rm H\,I}/M_\star$ in Section 4.

### 3.3 Dust-to-H I ratios

The $M_{\rm dust}/M_{\rm H\,I}$ ratio (or dust-to-gas ratio, if the contribution from molecular gas can be marginalized[3]) of a galaxy measures how many metals have been locked up in dust grains compared to the metals in the gas phase. To verify the reliability of this proxy, we plot the $M_{\rm dust}/M_{\rm metals}$ ratio (see Section 3.4) as a function of the $M_{\rm dust}/M_{\rm H\,I}$ ratio in Fig. 7 (right-hand panel), which shows a strong correlation ($\rho = 0.88$) with little scatter ($\sigma = 0.11$) around the best-fitting trend.

The $M_{\rm dust}/M_{\rm H\,I}$ ratios of our nearby galaxy samples range between $10^{-1.1}$ and $10^{-4.3}$ with a median $10^{-2.3\,\pm\,0.4}$ (see Fig. 4) that is roughly consistent with the Milky Way dust-to-H I gas column density ratio assumed in the THEMIS dust model (1/135; Jones et al. 2017). The $M_{\rm dust}/M_{\rm H\,I}$ ratio decreases with decreasing stellar mass ($\rho = 0.51$), and with increasing sSFR ($\rho = -0.41$), which is consistent with the consensus that less massive galaxies are currently in the process of vigorously forming stars, and that most of their metals have not been locked up in dust grains in comparison to the large reservoir of gas. In particular, HAPLESS (log $M_{\rm dust}/M_{\rm H\,I} = -2.59 \pm 0.23$)

---

[3] We note that for 44 KINGFISH and 81 HRS galaxies with CO data the median H$_2$/H I ratio is equal to 0.62 and 0.31, respectively, assuming a Galactic $X_{\rm CO}$ factor. For a metallicity- and luminosity-dependent $X_{\rm CO}$ factor, the median H$_2$/H I ratio for KINGFISH and HRS galaxies changes to 1.90 and 0.30, respectively. For HRS galaxies, these values are in line with the average $M_{\rm H_2}/M_{\rm H\,I}$ ratio of 0.3 for xGASS galaxies with stellar masses above $10^{10}$ M$_\odot$ (Catinella et al. 2018).

Downloaded from https://academic.oup.com/mnras/article/496/3/3668/5850384 by University College London user on 24 September 2020

**Table 2.** The best-fitting relations (of the form $y = a \times x + b$) have been inferred based on linear regression fits using the IDL procedure `MPFITEXY`, which is based on the non-linear least-squares fitting package MPFIT (Markwardt 2009). In addition to JINGLE, KINGFISH, HAPLESS, and HiGH galaxies, only HRS galaxies with an H I deficiency lower than 0.5 (i.e. classified as non-deficient galaxies) have been considered. The observed scatter ($\sigma$) around each of the best-fitting relations has been inferred. The Spearman rank correlation coefficient, $\rho$, and corresponding $p$-value have been inferred from the IDL procedure r_correlate to quantify the degree of (non-)linear correlation between the various quantities.

| $x$ | $y$ | $a$ | $b$ | $\sigma$ | $\rho$ | $p$-value |
|---|---|---|---|---|---|---|
| log $M_\star$ | log $M_{\rm dust}/M_\star$ | $-0.22 \pm 0.01$ | $-0.62 \pm 0.11$ | 0.39 | $-0.39$ | $<10^{-6}$ |
| log $M_\star$ | log $M_{\rm H\,I}/M_\star$ | $-0.80 \pm 0.01$ | $7.42 \pm 0.12$ | 0.57 | $-0.64$ | $<10^{-6}$ |
| log $M_\star$ | log $M_{\rm dust}/M_{\rm H\,I}$ | $0.47 \pm 0.01$ | $-6.90 \pm 0.11$ | 0.33 | 0.51 | $<10^{-6}$ |
| log $M_\star$ | log $M_{\rm dust}/M_{\rm metals}$ | $0.19 \pm 0.01$ | $-2.54 \pm 0.09$ | 0.24 | 0.26 | $<10^{-6}$ |
| log sSFR | log $M_{\rm dust}/M_\star$ | $0.56 \pm 0.01$ | $2.85 \pm 0.15$ | 0.29 | 0.63 | $<10^{-6}$ |
| log sSFR | log $M_{\rm H\,I}/M_\star$ | $0.89 \pm 0.02$ | $8.47 \pm 0.15$ | 0.40 | 0.72 | $<10^{-6}$ |
| log sSFR | log $M_{\rm dust}/M_{\rm H\,I}$ | $-0.28 \pm 0.01$ | $-5.08 \pm 0.10$ | 0.37 | $-0.41$ | $<10^{-6}$ |
| log sSFR | log $M_{\rm dust}/M_{\rm metals}$ | $-0.29 \pm 0.01$ | $-3.54 \pm 0.11$ | 0.24 | $-0.32$ | $<10^{-6}$ |
| Metallicity | log $M_{\rm dust}/M_{\rm H\,I}$ | $2.27 \pm 0.06$ | $-21.89 \pm 0.55$ | 0.34 | 0.53 | $<10^{-6}$ |
| Metallicity | log $M_{\rm dust}/M_{\rm metals}$ | $0.40 \pm 0.14$ | $-4.10 \pm 1.18$ | 0.26 | 0.11 | $4 \times 10^{-2}$ |
| log $M_{\rm H\,I}/M_\star$ | log $M_\star$ | $-1.25 \pm 0.01$ | $9.27 \pm 0.01$ | 0.51 | $-0.65$ | $<10^{-6}$ |
| log $M_{\rm H\,I}/M_\star$ | log $M_{\rm dust}/M_\star$ | $0.49 \pm 0.02$ | $-2.55 \pm 0.01$ | 0.28 | 0.67 | $<10^{-6}$ |
| log $M_{\rm H\,I}/M_\star$ | log $M_{\rm dust}/M_{\rm metals}$ | $-0.37 \pm 0.01$ | $-0.84 \pm 0.01$ | 0.20 | $-0.61$ | $<10^{-6}$ |
| log $M_{\rm H\,I}/M_\star$ | Metallicity | $-0.25 \pm 0.01$ | $8.54 \pm 0.01$ | 0.15 | $-0.55$ | $<10^{-6}$ |
| log $M_{\rm H\,I}/M_\star$ | log $M_{\rm dust}/M_{\rm H\,I}$ | $-0.63 \pm 0.01$ | $-2.63 \pm 0.01$ | 0.28 | $-0.72$ | $<10^{-6}$ |
| log $M_{\rm dust}/M_{\rm H\,I}$ | log $M_{\rm dust}/M_{\rm metals}$ | $0.61 \pm 0.02$ | $0.75 \pm 0.04$ | 0.11 | 0.88 | 0.0 |

and HiGH (log $M_{\rm dust}/M_{\rm H\,I} = -2.61 \pm 0.45$) galaxies have median ratios at the low end of the entire nearby galaxy population, which might at first seem surprising given their 'normal' $M_{\rm dust}/M_\star$ ratios. Similar trends were found by da Cunha et al. (2010) and consecutive works (Cortese et al. 2012; Clark et al. 2015; De Vis et al. 2017a), and attributed to galaxies with low stellar masses and high sSFRs, currently forming dust (high $M_{\rm dust}/M_\star$), and still retaining large H I gas reservoirs (low $M_{\rm dust}/M_{\rm H\,I}$) for future star formation. JINGLE (log $M_{\rm dust}/M_{\rm H\,I} = -2.25 \pm 0.31$) and KINGFISH (log $M_{\rm dust}/M_{\rm H\,I} = -2.30 \pm 0.69$) galaxies have ratios that agree well with the general trend observed for the ensemble of nearby galaxies, while the overall HRS sample median (log $M_{\rm dust}/M_{\rm H\,I} = -2.17 \pm 0.47$) is increased due to the high ratios (log $M_{\rm dust}/M_{\rm H\,I} = -1.80 \pm 0.44$) observed for H I-deficient HRS galaxies. The latter high ratios agree with the findings of Cortese et al. (2016), and were attributed to the outside-in stripping of the ISM in these H I-deficient HRS galaxies (where the extended H I component is affected more than the dust and molecular gas). The lowest ratios ($-4.3 \leq M_{\rm dust}/M_{\rm H\,I} \leq -3.9$) have been observed for four irregular KINGFISH galaxies (NGC 2915, HoII, DDO053, and NGC 5408) characterized by low stellar masses, low metal abundances, high sSFRs, high specific H I gas masses and low specific dust masses, which makes them stand out from the average KINGFISH galaxy population and characterizes these galaxies as being at an early stage of evolution.

Trends of dust-to-gas ratios with metallicity reported in the literature show that the $M_{\rm dust}/M_{\rm H\,I}$ ratio is strongly linked to the evolutionary stage of galaxies with gradually more metals being locked up in dust grains (e.g. Rémy-Ruyer et al. 2014). The relation between $M_{\rm dust}/M_{\rm H\,I}$ as a function of oxygen abundance is shown in Fig. 5, and is best fitted with a superlinear trend (slope: $2.26 \pm 0.07$). For reference, the linear relation (with a fixed slope of 1) and superlinear trend (with a slope of $2.02 \pm 0.28$) from Rémy-Ruyer et al. (2014) are overlaid as yellow solid and dashed lines.[4] Our trend is consistent with the superlinear relation from Rémy-Ruyer et al. (2014), which might seem surprising at first as the linear relation from Rémy-Ruyer et al. (2014) was found adequate to explain the trends at metallicities $12 + \log{\rm (O/H)} \gtrsim 8$ and the superlinear trend was invoked to explain the behaviour at metallicities lower than this threshold. A $\chi^2$ goodness-of-fit test confirms that the linear fit from Rémy-Ruyer et al. (2014) does not provide a good fit to the data ($p$-value of 1), even when excluding galaxies below a metallicity threshold of $12 + \log{\rm (O/H)} = 8.4$. The $p$-value (0.25) inferred from our best fit suggests that the data are neither well described by a non-linear relation, which likely results from the limited metallicity range covered by our sample, and the large degree of scatter in the relation ($\sigma = 0.34$). We furthermore compare our best-fitting relation to the superlinear trend (slope of $2.15 \pm 0.11$) inferred by De Vis et al. (2019) for a sample of ~500 DustPedia galaxies for the same metallicity 'PP04' calibration,[5] but they included an estimation of the molecular gas content. The slope of our relation agrees well with their superlinear trend, but it is offset by 0.2–0.3 dex to higher dust-to-H I ratios, which can likely be attributed to the omission of the molecular gas content in our galaxy samples and/or to the different samples under study in both works. In another DustPedia paper, a metallicity-dependent $X_{\rm CO}$ factor is invoked to reproduce a linear relation between the dust-to-gas ratio and metallicity (Casasola et al. 2019), as frequently observed both on

---

[4] Note that we are only interested in a comparison of their slopes, as the normalization of these curves cannot be directly compared to our values due to the differences in the assumed metallicity calibration, scaling factor for the gas mass to include heavier elements, and dust opacities.

[5] Note that the use of a different metallicity calibration would still yield a superlinear trend, but with a slightly different slope and/or normalization (see table 4 from De Vis et al. 2019).

Downloaded from https://academic.oup.com/mnras/article/496/3/3668/5850384 by University College London user on 24 September 2020

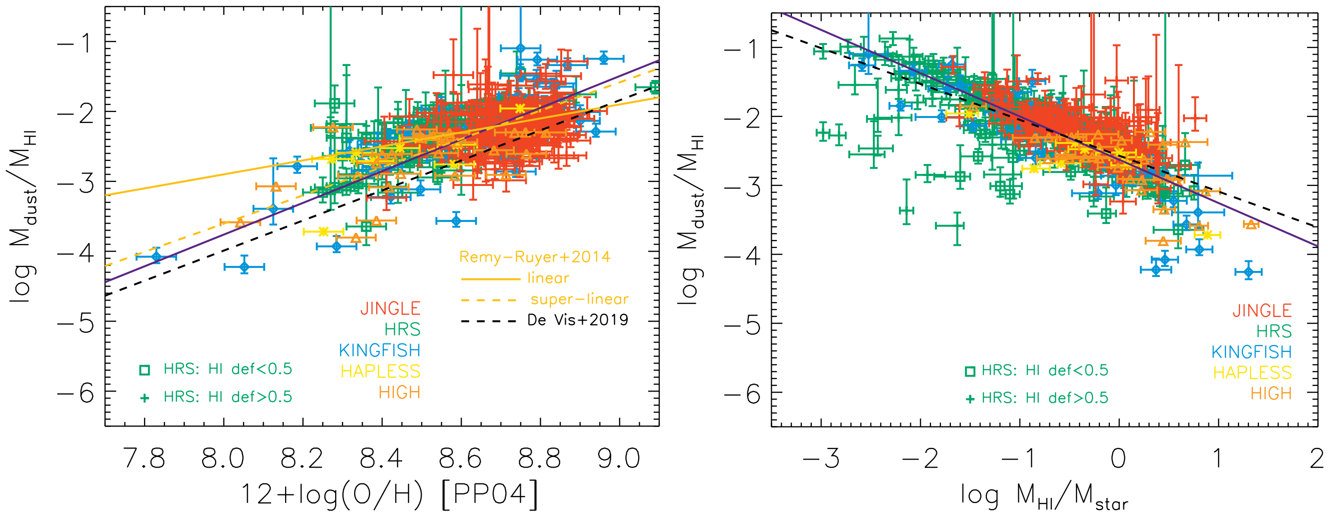

**Figure 5.** The scaling of the dust-to-H I mass ratio (i.e. $M_{\rm dust}/M_{\rm H\,I}$) with metallicity [as traced by the oxygen abundance 12 + log (O/H)] and the specific H I gas mass (i.e. $M_{\rm H\,I}/M_{\star}$). See the caption of Fig. 2 for more details on the symbols and plotted curves.

resolved and integrated galaxy scales in the local Universe (e.g. Lisenfeld & Ferrara 1998; Galametz et al. 2011; Magrini et al. 2011; Sandstrom et al. 2013). In future work, we will study the total gas scaling relations for JINGLE galaxies, and investigate the effect of different assumptions on the $X_{\rm CO}$ conversion factor. In the next paragraphs, we discuss the applicability of dust as a gas tracer based on the H I gas scaling relations of this work.

Dust mass measurements are often advocated as an alternative probe of the total ISM mass budget (e.g. Eales et al. 2012; Magdis et al. 2012; Scoville et al. 2014; Groves et al. 2015; Scoville et al. 2016; Janowiecki et al. 2018), due to the relative ease of obtaining IR data and inferring dust masses, as opposed to a combination of H I data (for which the sensitivity quickly drops at high redshifts) and CO observations (hampered by the notorious CO-to-$H_2$ conversion factor; Bolatto, Wolfire & Leroy 2013).

Fig. 5 shows that there is a considerable spread (0.34 dex) in the $M_{\rm dust}/M_{\rm H\,I}$ ratio as a function of oxygen abundance. The use of dust as an ISM mass tracer relies on the assumption of an approximately constant dust-to-gas ratio to convert dust masses into total gas masses. Variations of the dust-to-gas ratio with metallicity have been demonstrated before (e.g. Rémy-Ruyer et al. 2014), but the scatter around the best fit in Fig. 5 implies that the dust-to-H I ratio already varies by more than a factor of 2 at a fixed metallicity. In most cases, the metal abundances of galaxies are not known a priori, and the uncertainty on the estimated ISM mass reservoir will be higher than this factor of 2. Also the use of oxygen as a tracer of the total metal mass in galaxies might introduce an increased level of scatter. Some of the scatter in our relation might be caused by the missing molecular gas mass measurements, although Casasola et al. (2019) find that the H I gas mass correlates more closely to the dust mass than the molecular gas. Part of the spread might furthermore be attributed to the inhomogeneous extent of dust and gas reservoirs tracing different parts of a galaxy. In particular, JINGLE galaxies may be affected by the unresolved extent of H I gas observations obtained from single-dish observations. In due course, all JINGLE galaxies will be covered by future interferometric radio facilities (e.g. SKA, Apertif), which will give us a handle on the spatial extent of their H I gas reservoir. JINGLE, HAPLESS, and HiGH metallicities have furthermore been derived from the central 3 arcsec covered by SDSS fibre optical spectroscopy data (Thomas et al. 2013), which could potentially increase the uncertainty on their oxygen abundances due to the lack of a set of spatially resolved metallicity measurements, as opposed to the resolved metallicity measurements for the other nearby galaxy samples. Due to the wide spread in metallicity gradients observed in local galaxy samples (e.g. Kennicutt, Bresolin & Garnett 2003; Moustakas et al. 2010; Sánchez-Blázquez et al. 2014; Belfiore et al. 2017; Poetrodjojo et al. 2018; An 2019), these central metallicity measurements will not necessarily be representative of a galaxy's average metal abundance. Metallicity measurements (in particular at a low metallicity) furthermore come with large uncertainties due to the specific metallicity calibration that was applied, and its dependence on a fixed electron temperature in case of strong line calibrations. In addition, variations in the dust emissivity driven by an altered dust mineralogy or variations in carbon-to-silicate grain fractions (e.g. Clark et al. 2019) may be the cause of part of the scatter.

Janowiecki et al. (2018) argued that most of the scatter in the $M_{\rm dust}/M_{\rm H\,I}$ relation is driven by the unknown partition between atomic and molecular gas, and variations in the $H_2$-to-H I ratio with galaxy properties. Their study of the HRS galaxy sample suggests a dispersion of 0.22–0.25 dex in the relation between $M_{\rm dust}/M_{\rm H\,I}$ and metallicity, which is somewhat lower than the 0.34 dex scatter inferred for the sample of nearby galaxies in this paper.

### 3.4 Dust-to-metal ratios

We have calculated the dust-to-metal ratios (DTM) as the ratio of the dust mass and the total amount of metals (and thus accounting for metals in the gas phase and locked up in dust grains) similar to other literature works (e.g. De Vis et al. 2019):

$$\mathrm{DTM} = M_{\rm dust}/M_{\rm metals}(\mathrm{gas+dust}), \qquad (1)$$

with $M_{\rm metals}(\mathrm{gas + dust}) = f_Z \times M_{\rm gas} + M_{\rm dust}$. This prescription allows for a direct comparison with the measurements of dust depletion in damped Lyman $\alpha$ absorbers out to large redshifts (e.g. De Cia et al. 2016). The metal mass fraction $f_Z$ is calculated based on a galaxy's oxygen abundance, and the values of

Downloaded from https://academic.oup.com/mnras/article/496/3/3668/5850384 by University College London user on 24 September 2020

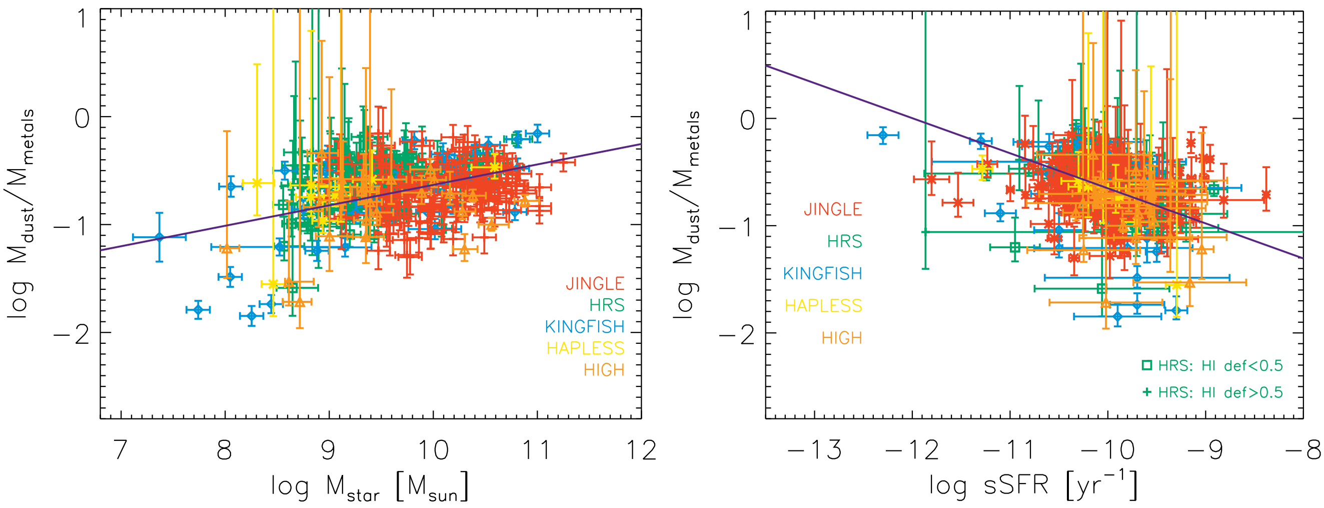

**Figure 6.** The scaling of the dust-to-metal mass ratio (i.e. $M_{\rm dust}/M_{\rm metals}$) with stellar mass ($M_\star$, left-hand panel) and specific star formation rate (sSFR with sSFR = SFR/$M_\star$, right-hand panel). See the caption of Fig. 2 for more details on the symbols and plotted curves.

the metal mass fraction ($f_{Z_\odot} = 0.0134$) and oxygen abundance [$12 + \log{\rm (O/H)}_\odot = 8.69$] inferred for the Sun from Asplund et al. (2009), which results in $f_Z = 27.36 \times 10^{12 + \log{\rm (O/H)} - 12}$. Due to the lack of molecular gas mass estimates, we have used the H I gas mass (corrected for the contribution from elements heavier than hydrogen; see equation D5) to calculate the metal mass fractions. We inferred that the DTM ratios are lower by −0.11 and −0.19 dex for 81 HRS and 44 KINGFISH galaxies, respectively, if we account for molecular gas masses assuming a Galactic $X_{\rm CO}$ conversion factor. A metallicity-dependent $X_{\rm CO}$ conversion factor would lower the DTM ratios by −0.46 dex for the KINGFISH sample (which contains the lowest metallicity galaxies in our local galaxy sample). It is worth noting that the metal mass furthermore relies on measurements of the oxygen abundance, which does not necessarily scale linearly to the total mass of metals in galaxies at different stages of evolution.

The DTM ratio provides a measure of the relative fraction of metals in the ISM that have been locked up in dust grains, and therefore sensitively depends on the efficiency of various dust production and destruction mechanisms. It is assumed that the DTM ratio remains more or less constant if dust is predominantly produced via stellar sources.[6] If grain growth dominates the dust production, the DTM ratio is thought to increase as galaxies evolve and their ISM is enriched with metals,[7] with grain growth believed to be more efficient than stellar dust production sources once a critical metallicity threshold has been reached (Asano et al. 2013). Dust destruction through supernova shocks (where metals locked up in dust grains are returned to the ISM) has the opposite effect and will lower the DTM ratio.

The majority of nearby galaxies fall within the same range of DTM ratios ($-0.90 \leq \log {\rm DTM} \leq -0.40$), with little variation among the different galaxy populations (see Table 1 and Fig. 6). The Milky Way is situated on the high end of this range with log DTM = −0.45, if we have assumed a total gas mass $M_{\rm gas} = 12.5 \times 10^9\,{\rm M}_\odot$ (Kalberla & Kerp 2009), solar metallicity, and dust-to-H I ratio of 1/135 as inferred from the Milky Way THEMIS model (Jones et al. 2017). The median ratio for HiGH galaxies (log DTM = −0.78 ± 0.30) is slightly lower than the other galaxy populations (but not significantly different; see Table E1) and confirms their early stage of evolution. The second lowest ratio (log DTM = −0.67 ± 0.23) is observed for JINGLE galaxies, but similarly does not differ significantly from HAPLESS (log DTM=−0.65 ± 0.15) and KINGFISH (log DTM = −0.63 ± 0.38) galaxies. The median ratio for HRS galaxies (log DTM = −0.60 ± 0.21) is significantly higher than that for the other four samples due to the contribution from H I-deficient HRS galaxies, with the latter being characterized by significantly higher ratios (log DTM = −0.44 ± 0.08). This DTM is more than 60 per cent higher than the median DTM observed in our sample of nearby galaxies (log DTM = −0.66 ± 0.24, excluding the H I-deficient HRS galaxies). This high DTM ratio appears consistent with the high $M_{\rm H_2}/M_{\rm dust}$ ratios observed in H I-deficient HRS galaxies (Cortese et al. 2016), and a picture of outside-in stripping of interstellar material where metals and H I are more easily stripped compared to the more centrally concentrated dust and molecular gas content. The median ratio for our nearby galaxy sample is higher than the average log DTM = −0.82 ± 0.23 from De Vis et al. (2019), which we attribute to the fact that we did not consider molecular hydrogen measurements. Indeed, we discussed earlier that neglecting the molecular gas content will overestimate the DTM ratios by 0.11 dex up to 0.46 dex.

We observe weak (but significant) correlations between the DTM and $M_\star$ ($\rho = 0.26$), sSFR ($\rho = -0.32$), and $M_{\rm H\,I}/M_\star$ ($\rho = -0.61$) (see Figs 6 and 8), while the relation with metallicity does not reveal a clear trend ($\rho = 0.11$; see Fig. 7, left-hand panel). These weak correlations suggest that the DTM increases as a galaxy evolves, although there is quite some scatter in these relations. In particular, galaxies with $M_\star \geq 10^9\,{\rm M}_\odot$ appear characterized by a nearly constant DTM, while the DTM drops significantly for several low-mass galaxies ($M_\star < 10^9\,{\rm M}_\odot$). This sudden change in DTM becomes particularly evident for less evolved galaxies with $\log M_{\rm H\,I}/M_\star > 0.3$ (see Fig. 8, bottom right panel), and has been

---

[6] This statement relies on the assumption that stellar dust yields, dust condensation efficiencies, and reverse shock destruction rates do not have a strong metallicity dependence.

[7] This inference is somewhat model dependent, and is also influenced by grain destruction efficiencies.

Downloaded from https://academic.oup.com/mnras/article/496/3/3668/5850384 by University College London user on 24 September 2020

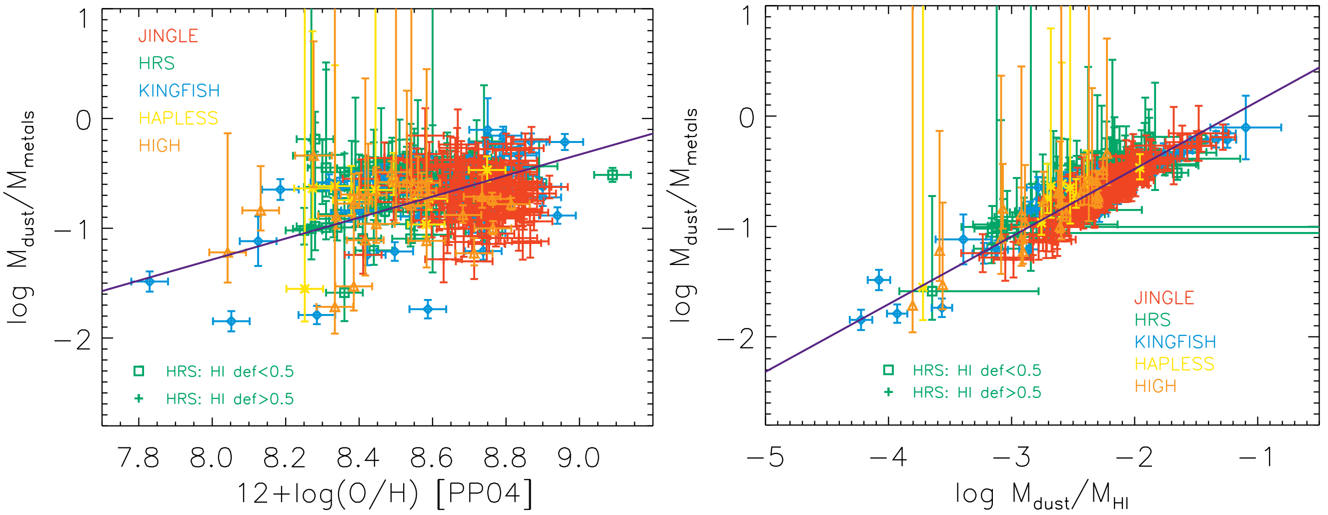

**Figure 7.** The scaling of the dust-to-metal mass ratio (i.e. $M_{\rm dust}/M_{\rm metals}$) with oxygen abundance [12 + log (O/H), left-hand panel] and dust-to-H I mass ratio (i.e. $M_{\rm dust}/M_{\rm H\,I}$, right-hand panel). See the caption of Fig. 2 for more details on the symbols and plotted curves.

attributed in the past to a critical metallicity threshold above which grain growth becomes efficient and contributes significantly to the dust production in galaxies (e.g. Asano et al. 2013). The absence of a clear trend with metallicity due to the large scatter in DTM ratios at low metallicities might suggest that this critical metallicity threshold can vary from one galaxy to another (Asano et al. 2013) or, alternatively, that such a critical metallicity threshold is not relevant.[8] In Section 4, we show that efficient grain growth is not required as a dominant dust production source to explain the current dust budgets of nearby galaxies with $-1.0 \lesssim \log M_{\rm H\,I}/M_\star \lesssim 0$. With supernova shock destruction releasing elements back into the gas phase, a wide range of DTM ratios (at a fixed metallicity) can also result from variations in dust destruction efficiencies and/or recent supernova rates. Also, the structure of the ISM and the filling factor of different ISM phases can play an important role in determining how efficiently grains can grow in the ISM, and how effectively supernova shocks can act as dust destroyers (Jones & Nuth 2011), and will add to the scatter.

To summarize our observational findings from these scaling relations, we infer that $M_{\rm H\,I}/M_\star$ varies considerably at a fixed stellar mass and fixed sSFR, more so than the $M_{\rm dust}/M_\star$ and $M_{\rm dust}/M_{\rm H\,I}$ ratios. This large spread can be interpreted as the specific H I gas mass being the main driver of the trends and scatter observed in other scaling laws (rather than variations in the relative contributions from several dust formation and destruction processes at a fixed stellar mass or sSFR). This picture is reinforced by the significant correlations between $M_{\rm H\,I}/M_\star$, and $M_{\rm dust}/M_\star$, $M_{\rm dust}/M_{\rm metals}$(gas + dust), and $M_{\rm dust}/M_{\rm H\,I}$ (see Fig. 8) and establishes that $M_{\rm H\,I}/M_\star$ is closely linked to the enrichment of the ISM with dust and metals, and the evolution of a galaxy, in general. In Section 4, we will interpret the evolutionary trends for $M_{\rm dust}/M_\star$, $M_{\rm dust}/M_{\rm H\,I}$, and $M_{\rm dust}/M_{\rm metals}$(gas + dust) using a set of chemical evolution models to infer what dust production and destruction mechanisms have contributed to build up a galaxy's present-day dust and metal budget.

## 4 INTERPRETING LOCAL SCALING LAWS WITH DEUS

### 4.1 Binning the sample in an evolutionary sequence

For the purpose of understanding how the dust, H I gas, and metal content evolves in galaxies, we have divided our local galaxy sample[9] into six separate bins according to equally sized ranges covered by galaxies in log $M_{\rm H\,I}/M_\star$. This subdivision results in unequal galaxy sample sizes in each bin. We decided to take this approach as the spread in various quantities (and thus the uncertainty on our median bin values) does not depend on the number of galaxies in each bin, but rather on the intrinsic scatter for galaxies at different stages of evolution. Table 3 lists the sample size, average stellar mass (log $M_\star$), specific H I gas mass [log ($M_{\rm H\,I}/M_\star$)], specific dust mass [log ($M_{\rm dust}/M_\star$)], dust depletion {log [$M_{\rm dust}/M_{\rm metals}$(gas + dust)]}, and metallicity for these six galaxy bins. The bins range from galaxies with high $M_{\rm H\,I}/M_\star$ ratios and thus at an early stage of evolution (Bin 1), down to galaxies with low $M_{\rm H\,I}/M_\star$ ratios, which have converted most of their gas into stars during the course of their lifetime (Bin 6).

### 4.2 DEUS modelling framework

To interpret what drives the evolution of the stellar mass, metal mass, H I gas, and dust content as galaxies evolve, we have used a Bayesian modelling framework to find the set of parameters capable of reproducing the observed scaling relations in the local Universe. To compare dust, H I gas, and metal scaling relations in the local Universe to model predictions, and infer what physical processes drive the observed trends and differences between galaxy populations, we have used a chemical evolution model that tracks the build-up and evolution of dust, gas, and metals throughout

---

[8] We should note that the metallicity range in our local galaxy sample is limited [with only one galaxy below 12 + log (O/H)<8.0] and might not reach down to the metallicity regime where a threshold would occur.

[9] We omitted H I-deficient HRS galaxies, since they have experienced recent removal of large fractions of their gas content, which makes it tenuous to reproduce their current H I gas, dust, and metal content without detailed constraints on the time-scale and the extent of their gas removal.

Downloaded from https://academic.oup.com/mnras/article/496/3/3668/5850384 by University College London user on 24 September 2020

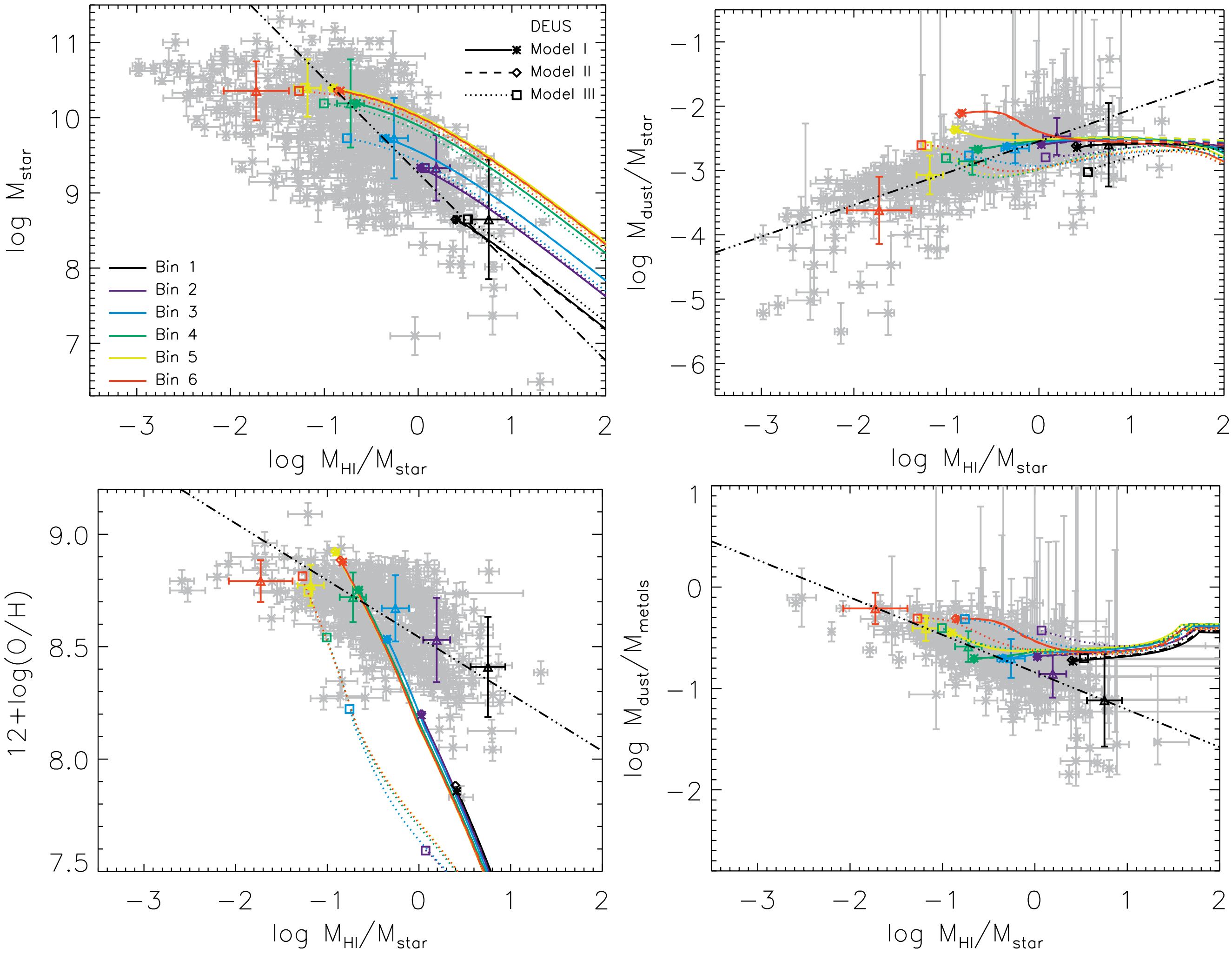

**Figure 8.** The scaling of the stellar mass ($M_\star$, top left), $M_{\rm dust}/M_\star$ (top right), oxygen abundance (bottom left), and $M_{\rm dust}/M_{\rm metals}$(gas + dust) (bottom right) with specific H I gas mass ($M_{\rm H\,I}/M_\star$) shown for our entire sample of nearby galaxies (grey symbols), with the best-fitting trends overlaid as black dashed–triple dotted lines. The median values for each of the six galaxy bins are overlaid with coloured triangles and errors that correspond to the spread in each bin. The $M_{\rm H\,I}/M_\star$ ratio is highest for galaxies in Bin 1 (which are thought to correspond to the least evolved galaxies), while the more evolved galaxies with the lowest $M_{\rm H\,I}/M_\star$ ratios populate Bin 6. The evolutionary trends (over a period of 12 Gyr) that were inferred from the median parameters for Models I, II, and III are overlaid as solid, dashed, and dotted lines, respectively, and the final present-day model values are indicated with coloured asterisks, diamonds, and squares, respectively. The colour coding of model trends and observed median properties ranges from black to red corresponding to Bins 1 through to 6 (see the legend in the top left panel).

**Table 3.** The bin number (1st column), log ($M_{\rm H\,I}/M_\star$) range (2nd column), sample size (3rd column), and median properties (columns 4–9) inferred for each of the six galaxy bins. These galaxy bins were selected to include less evolved galaxies (Bin 1) while gradually moving to galaxies with the most advanced stages of evolution (Bin 6).

| Bin | Range | $N_{\rm gal}$ | log ($M_\star$/M$_\odot$) | log (sSFR/yr$^{-1}$) | log ($M_{\rm H\,I}/M_\star$) | log ($M_{\rm dust}/M_\star$) | log ($M_{\rm dust}/M_{\rm metals}$) | Metallicity |
|---|---|---|---|---|---|---|---|---|
| 1 | [0.5, 1.3] | 17 | 8.65 ± 0.79 | − 9.36 ± 0.28 | 0.75 ± 0.19 | − 2.60 ± 0.65 | − 1.12 ± 0.46 | 8.41 ± 0.22 |
| 2 | [0, 0.5[ | 81 | 9.33 ± 0.44 | − 9.62 ± 0.29 | 0.19 ± 0.15 | − 2.47 ± 0.29 | − 0.86 ± 0.23 | 8.53 ± 0.19 |
| 3 | [−0.5, 0[ | 134 | 9.73 ± 0.53 | − 9.98 ± 0.35 | − 0.26 ± 0.15 | − 2.66 ± 0.23 | − 0.70 ± 0.19 | 8.67 ± 0.15 |
| 4 | [−1.0, −0.5[ | 132 | 10.19 ± 0.59 | − 10.21 ± 0.34 | − 0.72 ± 0.14 | − 2.86 ± 0.21 | − 0.59 ± 0.15 | 8.72 ± 0.11 |
| 5 | [−1.5, −1.0[ | 46 | 10.40 ± 0.38 | − 10.57 ± 0.63 | − 1.18 ± 0.14 | − 3.07 ± 0.30 | − 0.41 ± 0.12 | 8.77 ± 0.10 |
| 6 | [−3.0, −1.5[ | 13 | 10.36 ± 0.39 | − 11.30 ± 0.91 | − 1.72 ± 0.35 | − 3.62 ± 0.52 | − 0.21 ± 0.15 | 8.79 ± 0.09 |

the lifetime of a galaxy. More specifically, we employ DEUS, which accounts for dust production by AGB stars, supernova remnants (SNRs), grain growth in the ISM, and dust destruction through astration and processing by supernova shocks. Our model implementation is largely founded upon chemical evolution models presented in the literature (e.g. Dwek 1998; Morgan & Edmunds 2003; Calura, Pipino & Matteucci 2008; Rowlands et al. 2014). An earlier version of DEUS was introduced by De Looze et al. (2017b).

Downloaded from https://academic.oup.com/mnras/article/496/3/3668/5850384 by University College London user on 24 September 2020

We extended DEUS to include dust destruction by supernova shocks and dust growth in the ISM. We furthermore coupled DEUS to a Bayesian Markov chain Monte Carlo (MCMC) algorithm to study the effects of varying dust production and destruction efficiencies and to infer the set of parameters that best describes the observed scaling relations in the local Universe. In contrast to previous models (e.g. Pagel 1997; Dwek 1998), we have accounted for the lifetime of stars, and the replenishment of the ISM with metals, dust, and any remaining gas after stellar death, rather than resorting to the instantaneous recycling approximation for which the enrichment is assumed to occur at stellar birth. Appendix D gives a detailed overview of the DEUS code, our assumed metal and dust yields, and prescriptions for grain growth and dust destruction by supernova shocks. For this paper, we explore the following three different models:

(i) Model I assumes a closed-box and predicts the amount of dust and metals produced following the customized SFHs (see the next paragraph) inferred for the six galaxy bins.

(ii) Model II assumes a closed-box and adopts a fixed SFH shape for all six galaxy bins. More specifically, we have adopted a scaled version of the delayed SFH from De Vis et al. (2017b).

(iii) Model III deviates from the closed-box assumption, and includes gas infall and outflows (see Appendix D3), and furthermore relies on the customized SFHs inferred for each of the six galaxy bins.

The amount of metals and dust produced in galaxies sensitively depends on its (recent) star formation activity. Given that the six local galaxy samples correspond to different galaxy evolutionary stages, we expect them to have gone through different levels of recent star formation activity. To account for variations in their past and recent star formation activity, we have determined a customized SFH for each of the six galaxy bins by relying on their average stellar mass, sSFR, and SFR(10 Myr)-to-SFR(100 Myr) ratio. The latter SFRs were inferred from hybrid SFR calibrators: H $\alpha$+WISE 22 $\mu$m for SFR(10 Myr) and far-ultraviolet (FUV) + total-infrared (TIR) emission for SFR(100 Myr). The customized SFHs are presented in Appendix C, where it is demonstrated that galaxies at an early stage of evolution have formed most stars during recent epochs, as opposed to more evolved galaxies that show a clear drop in their recent star formation activity.

Due to possible degeneracies between various dust production and destruction sources, we have coupled DEUS to a Bayesian MCMC method to effectively search a large parameter space and to constrain the relative importance of stellar dust production, grain growth, and dust destruction by supernova shocks. Our Bayesian model has the following four free parameters: (1) the initial gas mass, $M_{\rm gas,\,ini}$; (2) the fraction of supernova dust that is able to survive the reverse shock, $f_{\rm survival}$; (3) the grain growth parameter, $\epsilon$ (see equation D11); and (4) the interstellar mass cleared by each single supernova event, $M_{\rm cl}$ (see equation D10), which is indicative of the dust destruction efficiency through supernova shocks. We leave the initial gas mass ($M_{\rm gas,\,ini}$) of the halo as a free parameter in DEUS to infer what gas mass is needed to reproduce the observed present-day specific H I gas masses ($M_{\rm H\,I}/M_{\star}$) and oxygen abundances. The initial gas mass is degenerate with the mass-loading factors of infalling and outflowing gas; we therefore constrain the initial gas mass in our models at fixed in- and outflow rates (or no gaseous flows in the case of Models I and II). In a similar way, variations in the initial gas mass are hard to differentiate from merger events occurring throughout a galaxy's lifetime. To constrain the free parameters in DEUS, we have compared the present-day model output to five observational quantities: log $M_{\star}$, log $M_{\rm dust}/M_{\star}$, log $M_{\rm H\,I}/M_{\star}$, log $M_{\rm dust}/M_{\rm metals}$(gas+dust), and 12 + log (O/H).[10]

As nothing much is known about the preferred values and their expected distribution, we have assumed flat priors to avoid biasing the model output results with log ($M_{\rm gas,\,ini}$/M$_{\odot}$) varying between 8.5 and 11, $f_{\rm survival}$ between 0.1 and 1.0, log ($\epsilon$) between 0.1 and 4.0, and log ($M_{\rm cl}/M_{\odot}$) between 0.1 and 5.0. This four-dimensional parameter space was sampled with an affine invariant ensemble sampler (Goodman & Weare 2010) as implemented in the `emcee` package for MCMC in `Python` (Foreman-Mackey et al. 2013). We have used a collection of 100 walkers to sample the entire parameter space, where the position of a walker is changed at each step to explore the parameter space and to look for a region with high likelihood. We assumed a likelihood function based on the commonly used $\chi^2$ statistic: $\chi^2 = \Sigma_{i=1}^{N}\left(\frac{f_{\rm i}({\rm obs}) - f_{\rm i}({\rm model})}{\sigma_{\rm i(obs)}}\right)^2$ with $f_{\rm i}$(obs) and $f_{\rm i}$(model) the observed and modelled values, respectively, and $\sigma_{\rm i(obs)}$ the observational uncertainty, for constraint i, which is equivalent to a Gaussian likelihood. The positions of the 100 walkers are recorded at each time-step after a warm-up phase of $N_{\rm burn}$ = 500 steps, and the simulations are run for a total of $N_{\rm steps}$ = 1500 steps. The final 1000 time-steps are used to construct the posterior probability density functions (PDFs). We furthermore verified that these steps are sufficient for each of the model parameters to converge, which requires the effective sample size $N_{\rm eff}$ (= $N_{\rm chain}/\tau_{\rm int}$ with $N_{\rm chain}$ the length of the chain and $\tau_{\rm int}$ the integrated autocorrelation time of the chain) to be higher than 10 for all parameters. As an additional check, we verified that the acceptance fraction of walkers ranges between 0.2 and 0.5.

### 4.3 Modelling results

The median parameter values inferred from the 1D posterior PDFs were tabulated in Table 4 for the three different models. Figs G1–G18 present the 1D and 2D posterior PDFs for the six galaxy bins and Models I, II, and III, respectively. The evolutionary tracks – as determined from those median parameter values and spanning a time period of 12 Gyr – have furthermore been overlaid on the individual panels of Fig. 8.

The stellar mass and metal abundance gradually increases for all models as galaxies evolve. For Model III (with gaseous in/outflows), the metallicity increase is less steep compared to Models I and II due to metal-enriched outflows. Due to this slow metal enrichment, Model III is able to reproduce the low specific gas masses observed for more evolved galaxies in Bins 5 and 6. The DTM ratio (i.e. the amount of metals depleted on to dust grains) starts off at a plateau around 40 per cent in all models, indicative of dust being produced mainly by stars, and only a minor contribution from grain growth, in the early stages of galaxy evolution. After a few 100 Myr, the metal abundance and dust mass have increased sufficiently for grain growth to kick in. However, the DTM ratio in our models first drops due to grain destruction (i.e. supernova shocks and astration) dominating over grain growth processes. For more evolved galaxies (Bins 5 and 6), the DTM ratio continues to increase due to grain growth becoming more dominant than these dust destruction mechanisms. Similar

---

[10] We have compared the median observed values to the model predictions at the end of our simulations at a galaxy age of 12 Gyr (assuming that these galaxies started forming stars 12 Gyr ago).

Downloaded from https://academic.oup.com/mnras/article/496/3/3668/5850384 by University College London user on 24 September 2020

**Table 4.** The median values for the four DEUS parameters as inferred from three different models for each of the six galaxy bins. Models I and II correspond to closed-box models with optimized non-parametric SFHs and with a delayed SFH (with fixed shape), respectively (see Appendix C). Model III includes gaseous in- and outflows (see Appendix D3) and the specific set of non-parametric SFHs. The upper and lower limits on the model parameters have been inferred from the posterior PDFs as the 16th and 84th percentiles. In addition to these output model parameters, we calculated the reduced $\chi^2_{\rm red}$ statistic by comparing the observed values with the model predictions for the median parameters. We also inferred the fraction of dust produced through stellar sources ($f_{\rm stardust}$) and through accretion processes in the ISM ($f_{\rm graingrowth}$) throughout the galaxy lifetime, and at the current age of the galaxy (values between square brackets).

| Bin | Bin 1 | Bin 2 | Bin 3 | Bin 4 | Bin 5 | Bin 6 |
|---|---|---|---|---|---|---|
| Model parameters | Model I. 'Closed-box' model with specific non-parametric SFHs | | | | | |
| $\log\,(M_{\rm gas,\,ini}/{\rm M}_\odot)$ | $9.33^{+0.11}_{-0.11}$ | $9.77^{+0.08}_{-0.07}$ | $9.99^{+0.05}_{-0.04}$ | $10.36^{+0.03}_{-0.03}$ | $10.51^{+0.02}_{-0.02}$ | $10.48^{+0.03}_{-0.03}$ |
| $f_{\rm survival}$ (per cent) | $51^{+33}_{-21}$ | $60^{+26}_{-27}$ | $63^{+24}_{-25}$ | $65^{+22}_{-27}$ | $69^{+23}_{-35}$ | $61^{+27}_{-34}$ |
| $\log \epsilon$ | $2.0^{+1.2}_{-1.3}$ | $1.8^{+1.2}_{-1.1}$ | $1.6^{+1.0}_{-1.0}$ | $1.5^{+0.8}_{-0.9}$ | $2.2^{+1.0}_{-0.7}$ | $3.0^{+0.7}_{-0.8}$ |
| $\log\,(M_{\rm cl}/{\rm M}_\odot)$ | $2.2^{+1.2}_{-1.4}$ | $1.6^{+1.1}_{-1.0}$ | $1.6^{+1.0}_{-1.0}$ | $1.4^{+1.0}_{-0.9}$ | $1.5^{+1.7}_{-1.0}$ | $1.8^{+1.3}_{-1.0}$ |
| $\chi^2_{\rm red}$ | 9.6 | 5.0 | 1.2 | 1.6 | 11.0 | 15.5 |
| $f_{\rm stardust}$ (per cent) | 99 [91] | 98 [84] | 96 [69] | 93 [52] | 55 [8] | 30 [16] |
| $f_{\rm graingrowth}$ (per cent) | 1 [9] | 2 [16] | 4 [31] | 7 [48] | 45 [92] | 70 [84] |
| Model parameters | Model II. 'Closed-box' model with delayed SFHs | | | | | |
| $\log\,(M_{\rm gas,\,ini}/{\rm M}_\odot)$ | $9.33^{+0.11}_{-0.10}$ | $9.77^{+0.08}_{-0.07}$ | $9.99^{+0.05}_{-0.05}$ | $10.35^{+0.03}_{-0.03}$ | $10.50^{+0.02}_{-0.02}$ | $10.48^{+0.03}_{-0.03}$ |
| $f_{\rm survival}$ (per cent) | $50^{+32}_{-27}$ | $59^{+27}_{-26}$ | $63^{+24}_{-26}$ | $68^{+21}_{-27}$ | $66^{+24}_{-35}$ | $60^{+28}_{-33}$ |
| $\log \epsilon$ | $2.0^{+1.3}_{-1.3}$ | $1.7^{+1.0}_{-1.1}$ | $1.5^{+1.0}_{-0.9}$ | $1.5^{+0.8}_{-0.9}$ | $2.1^{+1.0}_{-0.7}$ | $3.0^{+0.7}_{-0.7}$ |
| $\log\,(M_{\rm cl}/{\rm M}_\odot)$ | $2.0^{+1.3}_{-1.3}$ | $1.7^{+1.0}_{-1.1}$ | $1.5^{+1.0}_{-0.9}$ | $1.4^{+0.9}_{-0.9}$ | $1.5^{+1.6}_{-1.0}$ | $1.8^{+1.4}_{-1.1}$ |
| $\chi^2_{\rm red}$ | 9.4 | 4.9 | 1.2 | 1.6 | 10.9 | 15.3 |
| $f_{\rm stardust}$ (per cent) | 99 [96] | 98 [91] | 96 [81] | 93 [66] | 57 [13] | 30 [11] |
| $f_{\rm graingrowth}$ (per cent) | 1 [4] | 2 [9] | 4 [19] | 7 [34] | 43 [87] | 70 [89] |
| Model parameters | Model III. Model with gas in/outflows and specific non-parametric SFHs | | | | | |
| $\log\,(M_{\rm gas,\,ini}/{\rm M}_\odot)$ | $9.43^{+0.13}_{-0.12}$ | $9.79^{+0.10}_{-0.10}$ | $9.84^{+0.04}_{-0.02}$ | $10.27^{+0.01}_{-0.01}$ | $10.45^{+0.01}_{-0.01}$ | $10.41^{+0.01}_{-0.01}$ |
| $f_{\rm survival}$ (per cent) | $51^{+32}_{-31}$ | $66^{+24}_{-37}$ | $57^{+31}_{-38}$ | $66^{+24}_{-38}$ | $56^{+31}_{-36}$ | $34^{+32}_{-36}$ |
| $\log \epsilon$ | $2.8^{+1.8}_{-1.9}$ | $4.0^{+1.3}_{-2.5}$ | $3.7^{+0.7}_{-0.8}$ | $2.7^{+1.0}_{-1.0}$ | $2.9^{+0.8}_{-0.6}$ | $3.2^{+0.6}_{-0.6}$ |
| $\log\,(M_{\rm cl}/{\rm M}_\odot)$ | $2.1^{+1.5}_{-1.4}$ | $1.9^{+1.3}_{-1.2}$ | $1.8^{+1.4}_{-1.2}$ | $1.6^{+1.5}_{-1.0}$ | $1.7^{+1.4}_{-1.1}$ | $1.7^{+1.2}_{-1.1}$ |
| $\chi^2_{\rm red}$ | 26.4 | 30.3 | 23.9 | 7.0 | 0.8 | 5.8 |
| $f_{\rm stardust}$ (per cent) | 99 [95] | 71 [33] | 54 [12] | 73 [10] | 57 [8] | 49 [17] |
| $f_{\rm graingrowth}$ (per cent) | 1 [5] | 29 [67] | 46 [88] | 27 [90] | 43 [92] | 51 [83] |

results have been inferred from galaxy simulations (e.g. Aoyama et al. 2017). The dust-to-stellar mass ratio shows a similar trend with a nearly flat ratio at the start due to dust forming as stars evolve, progressing to a gradual increase (if grain growth starts to become important) or decrease (if dust destruction processes dominate).

In most cases, the present-day model values (indicated with asterisks, diamonds, and squares for Models I, II, and III, respectively, in Fig. 8) are capable of reproducing the observed ratios in each bin within the error bars (reflecting the dispersion observed within each $M_{\rm H\,I}/M_\star$ bin), which makes us confident that the models are adequate to reproduce the dust, metal, and H I gas scaling relations observed for the local Universe. There are, however, two notable exceptions. For evolved galaxy populations (Bins 5 and 6), Models I and II are not capable of reproducing their low observed specific H I gas masses ($\log M_{\rm H\,I}/M_\star \lesssim -1.0$). We believe this model discrepancy is driven by the closed-box assumption in Models I and II, as Model III is capable of reproducing the $M_{\rm H\,I}/M_\star$ ratios and metal abundances for these more evolved galaxies better. Due to their decrease in recent ($\lesssim$100 Myr) star formation activity, these galaxies are likely to have experienced some type of quenching during the last stages of their evolution. The assumption of a constant SFR on time-scales >100 Myr, with a sudden drop in their recent star formation activity might therefore not be fully representative if quenching time-scales are longer. However, the rapid star formation quenching inferred for several HRS galaxies (Ciesla et al. 2016) suggests that at least some galaxies experience a sudden drop in their SF activity on 100 Myr time-scales. A discrepancy is also observed for galaxies at an early stage of evolution (Bins 1 and 2), for which both closed-box models and models with gaseous flows underestimate the observed metal abundances (see the bottom panels in Fig. 8). We speculate that these modelled low metal abundances might be compensated for by locking fewer metals into dust grains – either through less efficient grain growth processes or more efficient grain destruction – which will also bring the modelled DTM ratios closer to the observed values. Other than possible model discrepancies, we should note that the oxygen abundances are missing for several galaxies at the low end of the metallicity range, which will inevitably bias our average bin measurements upwards for these less evolved galaxies as the full dynamic range of metallicity values has not been covered.

### 4.4 Dust production and destruction efficiencies

In the rest of the paper, we focus our discussion on the dominant dust production and destruction mechanisms for the subsample of galaxies in Bins 3 and 4 with $-1.0 \lesssim \log M_{\rm H\,I}/M_\star \lesssim 0$, which constitute the majority (266/423 or 63 per cent) of the local galaxy population. Stochastic effects will not hamper the median values

Downloaded from https://academic.oup.com/mnras/article/496/3/3668/5850384 by University College London user on 24 September 2020

inferred for the galaxies in Bins 3 and 4 as is the case for poorly sampled galaxy bins at the low- and high-$M_{\rm H\,I}/M_\star$ end. The stellar mass range ($10^9$–$10^{11}$ M$_\odot$) covered by Bins 3 and 4 furthermore corresponds to galaxies in which an equilibrium is reached between gaseous infall, outflow, and star formation (Bothwell et al. 2013). Such an equilibrium implies that the choice of specific gas infall/outflow rates and mass-loading factors for these galaxies will have less of an impact on the output model parameters. The galaxies outside this stellar mass range instead show a large degree of scatter, and will be more sensitive to the effect of gas infall or outflows during recent times. We prefer to focus on these galaxies, for which the effect of gas infall or outflows during recent times has been less important, having sustained star formation over several Gyr (see Fig. C1). The closed-box Models I and II result in adequate fits (as quantified by the $\chi^2_{\rm red}$ statistic; see Table 4) for these galaxies at an intermediate stage of evolution. We note that the conclusions for Models III (including gaseous in/outflows) generally remain unmodified, but these models typically give rise to larger model parameter uncertainties and less well constrained fits (see Table 4) due to the increased level of model complexity. Specifically, the oxygen abundance is severely underestimated due to the recent infall of pristine gas for galaxy Bins 1 through to 4, which results in higher $\chi^2_{\rm red}$ values for Model III than those for Models I and II. The specific prescription adopted here to model gaseous flows might not be appropriate for the entire range of galaxies in our sample, and there result in worse model fits to the data. The assumed infall and outflow rates in Model III fit the data well for galaxies in Bins 5 and 6, resulting in better fits than for Models I and II.

### 4.4.1 *Initial gas mass*

The initial gas masses are well determined showing peaked 1D posterior PDFs with values that gradually increase with the evolutionary stage of galaxies (see Table 4) in line with the expectation that galaxies at an advanced stage of evolution are more massive, and thus require a larger initial mass to convert gas into stars than less evolved galaxies. It should be noted that part of this trend might be driven by merger events leading to increased gas masses at specific times throughout a galaxy lifetime rather than increased initial gas masses. Since these merger events have not been considered here, the models may have converged to large initial gas masses to reproduce present-day scaling laws for more evolved galaxies. The initial gas masses might be one of the most important parameters in DEUS as they directly influence the present-day model stellar masses and metal abundances, and play an important role in setting the posterior PDFs obtained for the other parameters. In future work, we intend to explore the importance of the initial gas mass parameter (and possible degeneracies with gaseous in- and outflows and merger events) in more detail.

### 4.4.2 *Net supernova dust production rates*

Models I and II suggest that a significant fraction (37–89 per cent) of freshly condensed supernova dust is able to survive the reverse shock. Dust evolution models that include the effects of sputtering and/or shattering on supernova dust grains due to the passage of a reverse shock estimate dust survival rates ranging from 1 to 100 per cent (e.g. Bianchi & Schneider 2007; Nozawa et al. 2007; Nath, Laskar & Shull 2008; Silvia, Smith & Shull 2010; Sarangi & Cherchneff 2015; Biscaro & Cherchneff 2016; Bocchio et al. 2016; Micelotta, Dwek & Slavin 2016; Kirchschlager et al. 2019). An easy comparison between these various models is hampered by the different assumptions made to describe the ambient densities, the density contrast between dust clumps and the surrounding medium, the grain size distribution, and the composition of supernova dust species. In addition, our inferred dust survival rate will account for the fact that some SNRs will not experience a reverse shock (e.g. the Crab Nebula) due to the low density of the surrounding medium, and should thus be considered as an 'effective' dust survival rate as it is convoluted with the probability that a reverse shock will be generated through the interaction with a dense circum- or interstellar medium, and that dust might be able to reform after the shock passage (e.g. Matsuura et al. 2019). Current observational studies tend to be biased towards interacting SNRs or pulsar wind nebulae that provide a heating mechanism through shock interaction or through the presence of a pulsar, respectively. It is therefore hard to estimate the fraction of SNRs that will experience a reverse shock, and at what average velocity the reverse shock will interact with the ejecta. Moreover, a non-negligible fraction of core-collapse supernovae occur 'late' (i.e. 50–200 Myr after birth) due to binary interactions (Zapartas et al. 2017). On such long time-scales, the birth clouds of these massive stars will have dissolved, and it will become less likely that a reverse shock is generated.

Our high dust survival fractions are in excellent agreement with recent observational constraints. Elevated dust-to-gas ratios in the shocked ejectum clumps of the Galactic SNR Cassiopeia A suggest that a significant fraction of supernova dust is capable of surviving a reverse shock (Priestley, Barlow & De Looze 2019). Several studies (e.g. Temim & Dwek 2013; Gall et al. 2014; Wesson et al. 2015; Bevan & Barlow 2016; Priestley et al. 2020) have also argued for rather large supernova grain sizes ($\gtrsim$0.1 μm), which lends support to the idea that significant fractions of supernova dust are able to survive a reverse shock (with large grains being more resilient to sputtering, e.g. Silvia et al. 2010).

### 4.4.3 *Grain growth time-scales*

The grain growth parameter has been parametrized through $\epsilon$ following Mattsson, Andersen & Munkhammar (2012) (see equation D11 and Appendix D2 for an outline of its derivation). At a fixed gas mass, dust-to-gas ratio, metal fraction, and SFR, the grain growth parameter $\epsilon$ is inversely proportional to the grain growth time-scale, and can be considered to approximate the efficiency of grain growth processes. More specifically, large values of $\epsilon$ correspond to efficient grain growth and thus short grain growth time-scales $\tau_{\rm grow}$, while small $\epsilon$ values are indicative of long $\tau_{\rm grow}$.[11]

The 1D posterior PDFs for Models I and II, and Bins 3 and 4, have log $\epsilon$ peaking around 2.0, with a wide tail of high-likelihood models extending to lower log $\epsilon$ values and a sudden drop in likelihood beyond values of log $\epsilon \gtrsim 2.0$. The 1D posterior PDFs for Model III peak at higher values (see Figs G9 and G12) than those for closed-box models, which is not surprising given that dust and metals will be expelled from the galaxy, and thus an additional source of dust production is required in Model III. A narrow range of models with $\epsilon$ values higher than this peak seems also capable

---

[11] Values of $\epsilon$ of 10–100 typically correspond to $\tau_{\rm grow} > 100$ Myr, while $\epsilon \gtrsim 1000$ is needed to reach down to $\tau_{\rm grow}$ of 10 Myr and lower (depending on the assumed SFR, gas, dust, and metal mass).

Downloaded from https://academic.oup.com/mnras/article/496/3/3668/5850384 by University College London user on 24 September 2020

of explaining our observed scaling relations, but only if such high grain growth efficiencies are exactly compensated for by high dust destruction efficiencies (e.g. the rightmost 2D contour plot on the bottom row of Figs G10, G11, and G12). With grain growth locking refractory elements into grains, and dust destruction releasing these same elements back into the gas phase, our observational constraints are not capable of distinguishing between both mechanisms. The model prescriptions to describe grain growth and dust destruction efficiencies furthermore depend directly (or indirectly in case of the supernova rate) on the current SFR, which causes this degeneracy between grain growth and dust destruction efficiencies, as long as both processes cancel each other out. To adapt those recipes, we require improved understanding of the grain growth and destruction processes in the ISM. The 2D contour plots suggest that the models are also hampered by degeneracies between the supernova dust survival rate ($f_{\rm survival}$), the grain growth parameter ($\epsilon$), and the dust destruction efficiency ($M_{\rm cl}$) in some parts of the 4D parameter space, which results in wide 1D posterior PDFs.

Our median values of log $\epsilon = 1.5^{+1.1}_{-0.9}$ – equivalent to present-day growth time-scales $\tau_{\rm growth}$ of $\gtrsim$100 Myr, with a median of 400 Myr – are consistent with the range of values ($\epsilon \in$[10, 457]) inferred by Mattsson & Andersen (2012) based on the resolved DTM gradients observed in a sample of 15 SINGS galaxies, and the accretion time-scales ($\tau_{\rm grow}$ = 20–200 Myr or $\epsilon$ = 500) that were found adequate to reproduce the dust masses in a sample of high-redshift ($z$>1) submillimetre galaxies (Rowlands et al. 2014). In general, however, our grain growth efficiencies are significantly lower than those of many other studies. In Asano et al. (2013), Zhukovska (2014), Mancini et al. (2015), and Schneider et al. (2016), fast grain growth time-scales of 0.2–2 Myr have been assumed, which causes grain growth to dominate dust production as soon as a critical metallicity threshold has been reached. Feldmann (2015) required similarly short accretion time-scales (5 Myr) to reproduce the dust and metal masses in low-metallicity dwarf galaxies. Also the dust, metal, and gas scaling relations for a sample of nearby galaxies were found to be best reproduced by chemical evolution models with $\epsilon$ values of 2500–4000 (De Vis et al. 2017b).[12] All of these studies suggest that grain growth dominates dust production for different galaxy populations across a wide range of different redshifts (see also Section 4.5).

Even though recent laboratory studies suggest that $SiO_x$ and more complex silicate-type grains can form without an activation energy barrier under typical molecular cloud ($T_{\rm dust}$ = 10–12 K) conditions (Krasnokutski et al. 2014; Rouillé et al. 2015; Henning et al. 2018), it might be hard for the majority of dust grains in the low-redshift Universe to have formed through accretion of elements on to pre-existing grain seeds given the low accretion rates and the Coulomb barrier that needs to be overcome in diffuse gas clouds, and the efficient formation of ice mantles that prevents efficient grain growth in dense molecular clouds (Barlow 1978; Ferrara et al. 2016; Ceccarelli et al. 2018). Zhukovska et al. (2016) modelled the formation of silicate grains through the accretion of elements in diffuse gas clouds (with gas densities $n_{\rm H}$ between 5 and 50 cm$^{-3}$) on average time-scales of 350 Myr, while Zhukovska, Henning & Dobbs (2018) suggest that iron grains can grow efficiently in the cold neutral medium on time-scales of $\lesssim$10 Myr. Due to the absence of laboratory measurements of diffusion and desorption energies, the latter works assumed that elements sticking to grain surfaces will have sufficient time to reach a strong active bonding site where these refractory elements can be chemisorbed. Given that the exposure to strong UV radiation in diffuse gas clouds will make these elements prone to photodesorption processes, and various elements on the grain surface (with differing diffusion energies) might be competing for the same dangling bonds, we argue that a detailed set of laboratory studies, combined with detailed chemical modelling, is needed to verify what kind of grain species can form and what time-scales are involved in their formation. We speculate that our longer grain growth time-scales (and longer dust lifetimes; see Section 4.4.4) might reduce the tension with grain surface chemical models that have so far been incapable of proposing a viable chemical route for grain growth.

### *4.4.4 Dust destruction efficiencies*

The dust destruction efficiency has been parametrized through the interstellar mass that is cleared per single supernova event ($M_{\rm cl}$). In reality, it is unlikely that a single value will apply to all supernova events as $M_{\rm cl}$ will depend on the ambient density, on the 3D structure of the ambient medium, and on the supernova explosion energy. With several models assuming a single value for $M_{\rm cl}$, we pursue to infer what average values are adequate to reproduce the observed scaling laws in the local Universe. Similar to the grain growth parameter, the 1D posterior PDF for $M_{\rm cl}$ shows a sharp drop in likelihood beyond $M_{\rm cl} \gtrsim 10^{2.4}$ M$_{\odot}$. Higher values are only allowed in case the dust destruction efficiency is perfectly balanced by the same level of dust production through grain growth. The models are incapable of distinguishing between values of $M_{\rm cl}$ below this threshold due to degeneracies with the level of supernova dust production and the grain growth parameter.

The peaks in the 1D posterior PDFs occur at low $M_{\rm cl}$ values, resulting in median values of $M_{\rm cl} = 10^{1.4-1.6}$ for galaxies in Bins 3 and 4, and correspond to long dust lifetimes of 1–2 Gyr. The upper limits in our models for the mass cleared per supernova event ($\lesssim$400 M$_{\odot}$) are consistent with current dust destruction time-scales of $\gtrsim$200 Myr. Our preferred model dust lifetimes of a few Gyr are consistent with the longer dust destruction time-scales (2–3 Gyr) inferred for silicate grains by Slavin, Dwek & Jones (2015) by means of SNR models with evolving shock waves. Long dust lifetimes (of the order of a few Gyr) for silicate grains were also suggested by Jones & Nuth (2011) after accounting for the 3D distribution of interstellar material, while carbonaceous grains are assumed to be processed on short time-scales. Our conclusion applies to the ensemble of interstellar grains, and is in agreement with these longer silicate lifetimes. In future work, we hope to make the distinction in our models between the formation and destruction of various grain species such as carbonaceous and silicate dust grains. It is worth noting that our inferred dust destruction time-scales are factors of a few longer than the average values reported by other works (e.g. 400–600 Myr, Jones et al. 1994; Jones, Tielens & Hollenbach 1996; <90 Myr, Rowlands et al. 2014; 20–70 Myr for dust in the Magellanic clouds, Temim et al. 2015; Lakićević et al. 2015; 350 Myr, Zhukovska et al. 2016, 2018; Hu et al. 2019).

## 4.5 Dominant dust production sources

Our thorough search of the four-dimensional parameter space, adapted to cover a wide range of different Dust and Element evolUtion modelS, has revealed that local galaxy scaling relations (with

---

[12] The $\epsilon$ values (5000–8000) from De Vis et al. (2017b) have been corrected to account for their assumed cold gas fraction ($f_{\rm c}$ = 0.5) to allow for a direct comparison with our values.

Downloaded from https://academic.oup.com/mnras/article/496/3/3668/5850384 by University College London user on 24 September 2020

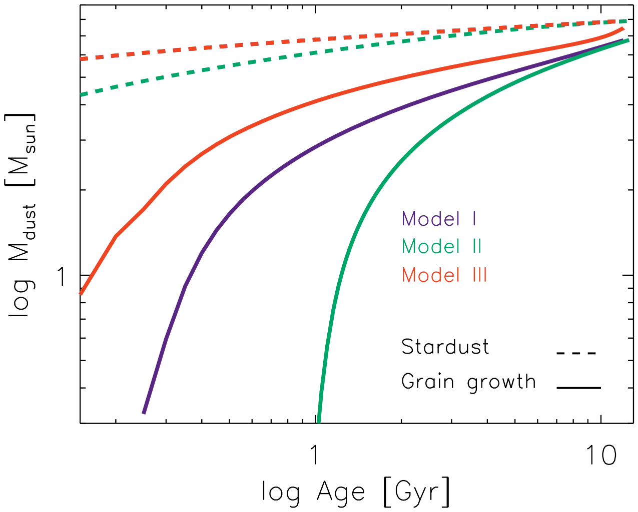

**Figure 9.** The amount of dust produced through stellar sources (AGB + SNe, dashed curves) and through interstellar grain growth (solid curves) as a function of galaxy age, as inferred from the median model parameter values for Bin 4. The stardust tracks for Model I and Model III overlap due to the same assumed SFH shape for both models.

the exception of galaxies with low and high specific gas masses) can be reproduced adequately by models with long dust survival rates (of the order of 1–2 Gyr), low grain growth efficiencies ($\epsilon$ ∼30–40), and a predominant contribution of stellar dust production sources to account for the present-day galaxy dust budgets. More specifically, we estimate that most of the dust (>90 per cent) is produced through stellar sources over a galaxy's lifetime, with a minor contribution from grain growth (<10 per cent; see Fig. 9). The contribution of grain growth increases with time for all models, with 50–80 per cent of present-day dust masses resulting from stellar dust, while 20–50 per cent of the dust is suggested to grow through the accretion in interstellar clouds. Models with in- and outflows (Model III) have an increased contribution from grain growth, resulting in more or less equal contributions from grain growth and stellar sources to the dust production over a galaxy lifetime. Given that a fraction of the dust is lost in galactic outflows (i.e. scaled with the dust-to-gas ratio of the galaxy at that point in time), we require more dust production through grain growth to reproduce the observed dust-to-stellar and dust-to-metal mass ratios with Model III. We furthermore note a trend of high relative fractions of stardust for less evolved galaxies (Bins 1 and 2), which is not surprising given the low metal abundances (and hence low grain growth efficiencies) for these galaxies.

We speculate that through performing a rigorous search of the four-dimensional parameter space, our results provide an alternative for the chemical evolution models with extremely low supernova dust production efficiencies and short grain growth time-scales ($\lesssim$a few Myr), which have been invoked to explain the dust, metal, and gas scaling laws of local galaxies (e.g. Zhukovska 2014; Feldmann 2015; De Vis et al. 2017b). Regardless of our model assumptions on the SFH and gaseous flows, the local dust, H I gas, and metal scaling relations are reproduced well with models that assume long dust lifetimes (1–2 Gyr), favourable supernova dust injection rates ($f_{\rm survival}$ of 37–89 per cent), and low grain growth efficiencies ($\epsilon$ of 30–40). These long grain growth time-scales could reduce the tension between the high grain growth efficiencies (required to reproduce the large dust masses observed in low- to high-redshift galaxies) and grain surface chemical models, which currently fail to account for efficient grain growth processes in the ISM (e.g. Barlow 1978; Ferrara et al. 2016; Ceccarelli et al. 2018; Jones & Ysard 2019).

### 4.6 Modelling caveats

We resorted to making some assumptions in DEUS to avoid introducing various model degeneracies. We briefly discuss the implications of these assumptions.

(i) SFH: We have assumed a customized SFH for each galaxy bin (i.e. Model I). To test the importance of this model assumption, we also ran models with a delayed SFH (i.e. Model II). A quick comparison between the inferred model parameters shows that the dependence on the specific shape of the SFH is minimal based on the close resemblance between the Model I and II output parameters (see Table 4). We argue that the minor importance of the specific SFH shape results from the long dust lifetimes, which imply that the current dust reservoir has been built up during the last 1–2 Gyr, and that variations in the SFH shape on these time-scales are less relevant as long as the final produced dust mass remains the same. We should also note that the simplicity of the SFH shapes, and other model assumptions, may affect the dependence of the results on the SFH.

(ii) Closed-box versus gaseous flows: Even though the importance of gaseous flows is now well established in the field, the precise nature of these gas-regulated 'bathtub' galaxies still requires further characterization. In Model III, we have assumed that the infalling gas is pristine (i.e. the gas is not enriched with metals or dust), while the outflowing gas has the same gas-phase metallicity and dust-to-gas ratio as the galaxy at the time of the outflow. This assumption will vary depending on the outflow mechanism and the location of the onset of these gaseous outflows. The outflow rate is often assumed to scale with the SFR, but a time-dependent outflow model with strong outflows at early times has been shown adequate to reproduce the observed gas and stellar metallicities in galaxies (Lian et al. 2018a). Similar time- or stellar mass-dependent outflows are also consistent with galaxy simulations (e.g. Muratov et al. 2015; Hayward & Hopkins 2017). We suggest that these strong outflows at early times (as implemented in our Model III) result in a slow build-up of a galaxy's metal content, which reduces the efficiency of grain growth processes at early times. Low outflow rates at the present epoch also reduce the need for short grain growth time-scales to account for the observed dust masses in galaxies. However, as remarked upon before, different assumptions on the time dependence of these outflows will affect dust production and destruction efficiencies. To limit these biases, we have assumed closed-boxes for Models I and II to model galaxies that have reached an equilibrium between gaseous infall, outflow, and star formation.

(iii) One-zone models: Outflow rates are thought to vary with radial distance from the galaxy centre (e.g. Lian et al. 2018b; Belfiore et al. 2019; Vílchez et al. 2019), which would require resolved galaxy models to take this into consideration. Other than these spatial variations in mass-loading factors, the 3D structure and filling factors of various ISM phases that together constitute an entire galaxy will vary depending on the evolutionary stage and the specific type of galaxies under consideration. Dwarf galaxies in the nearby Universe provide an excellent example of how their low metal and dust content, high degree of porosity, and radiation field hardness severely affect their ISM build-up with a highly ionized, diffuse medium that dominates the ISM volume, and only

Downloaded from https://academic.oup.com/mnras/article/496/3/3668/5850384 by University College London user on 24 September 2020

minor contributions from compact phases (e.g. Lebouteiller et al. 2012; Cormier et al. 2015, 2019; Madden & Cormier 2019). The detection of highly ionized nebular lines (e.g. Smit et al. 2014; Inoue et al. 2016; Carniani et al. 2017; Laporte et al. 2017; Hashimoto et al. 2018) suggests that high-redshift galaxies might have an ISM build-up similar to low-metallicity dwarfs in the nearby Universe, and supports the need for spatially resolved chemical evolution modelling to account for radially dependent gas in/outflows and filling factors of different ISM phases (e.g. Peters et al. 2017). In the future, we plan to expand DEUS to include a realistic 3D ISM structure to model how the density and temperature distributions of the total ensemble of gas clouds in a galaxy vary with time.

(iv) Metal and dust yields: We had to assume a set of AGB and supernova metal and dust yields, and apply specific prescriptions to describe the efficiency of grain growth and dust destruction processes. We endeavoured to select yields and recipes that are in line with the current state-of-the-art, but these prescriptions remain limited by our current knowledge on how grains are destroyed and whether or not grains can grow either in diffuse or dense clouds of the ISM. If the true yields were to differ significantly from our model assumptions and/or show variations with metallicity (e.g. Valiante et al. 2009; Boyer et al. 2019; Dell'Agli et al. 2019), this could impact our inferred model parameters. In De Vis in prep., the choice of metal yields is shown to mostly impact the metallicities of galaxies with high specific gas masses.

(v) Time dependence: We have not accounted for variations in the dust destruction efficiency and grain growth parameter in time, which could be induced if strong variations in the grain size distribution occur throughout a galaxy's lifetime, as the efficiency of grain destruction and grain growth is strongly grain size dependent (e.g. Hirashita 2015).

(vi) Initial mass function (IMF): We have furthermore assumed a fixed Chabrier (2003) IMF. The shape of the IMF has been suggested to vary in different environments (e.g. Oldham & Auger 2018), and deviations from this standard IMF will affect the dust and metal yields, and supernova rates in DEUS.

In future work, we aim to explore the effects of varying the IMF and applying different sets of metal and dust stellar yields, to accommodate physically motivated recipes to describe grain growth and dust destruction processes, and to allow for spatial variations in the efficiencies of these processes with local ISM conditions.

## 5 CONCLUSIONS

We analysed local dust, H I gas, and metal scaling relations for a diverse sample of 423 nearby galaxies to infer that:

(i) the specific dust and H I gas masses are tightly linked to a galaxy's sSFR, which suggests that the interstellar mass (either traced through H I gas or dust) plays an important role in setting a galaxy's SFR (through the Kennicutt–Schmidt law).

(ii) the H I gas scaling laws show the largest degree of dispersion, which suggests that variations in $M_{\rm dust}/M_{\star}$, $M_{\rm dust}/M_{\rm metals}$(gas + dust), and $M_{\rm dust}/M_{\rm H\,I}$ ratios are not necessarily influenced by dust production and destruction mechanisms but rather driven by the current H I gas reservoirs of galaxies.

(iii) the strong correlations between $M_{\rm H\,I}/M_{\star}$, and $M_{\rm dust}/M_{\star}$, $M_{\rm dust}/M_{\rm metals}$(gas + dust), and $M_{\rm dust}/M_{\rm H\,I}$ reinforce the idea that the specific H I gas mass ($M_{\rm H\,I}/M_{\star}$) plays an important role in setting the dust and metal content of galaxies.

(iv) the $M_{\rm dust}/M_{\rm metals}$(gas + dust) ratio in galaxies is nearly constant ($10^{-0.66\pm0.24}$) across our sample of galaxies for $M_{\star} \geq 10^9$ M$_{\odot}$. Weak (but significant) trends with $M_{\star}$, sSFR, and $M_{\rm H\,I}/M_{\star}$ support a scenario of increasing $M_{\rm dust}/M_{\rm metals}$(gas + dust) ratios as a galaxy evolves.

(v) the large spread (0.34 dex) in the $M_{\rm dust}/M_{\rm H\,I}$ ratio at a given metallicity should urge caution: Total gas masses inferred from dust mass measurements will be uncertain by a factor of $\gtrsim$2 due to variance – driven by intrinsic galaxy variations, the unknown extent of H I reservoirs and/or uncertain oxygen abundances – at a fixed metallicity.

To model the evolution of the dust and metal budgets in nearby galaxies, we have split up the local sample of galaxies in six 'galaxy evolutionary' bins according to their specific H I gas masses. The observed $M_{\star}$, metallicity, $M_{\rm dust}/M_{\star}$, $M_{\rm H\,I}/M_{\star}$, and $M_{\rm dust}/M_{\rm metals}$(gas + dust) ratios at these six galaxy evolutionary stages were interpreted with a set of Dust and Element evolUtion modelS (DEUS) – including dust production by AGB stars, SNRs, grain growth in the ISM, and dust destruction through astration and processing by supernova shocks. DEUS was coupled to an MCMC method to effectively search a large parameter space and to constrain the relative importance of stellar dust production, grain growth, and dust destruction by supernova shocks. We obtained an extensive set of models by varying the initial gas mass ($M_{\rm gas,\,ini}$), the survival rate of supernova dust after passage of the reverse shock ($f_{\rm survival}$), the grain growth parameter ($\epsilon$), and the interstellar mass cleared per supernova event ($M_{\rm cl}$, which determines the efficiency of dust destruction through supernova shocks). Based on a rigorous search of this four-dimensional parameter space, we conclude that:

(i) the average scaling laws for galaxies with $-1.0 \lesssim \log M_{\rm H\,I}/M_{\star} \lesssim 0$ (which are considered to have reached an equilibrium between gas infall, outflow, and star formation) can be reproduced using closed-box models with a high fraction (37–89 per cent) of supernova dust that is able to survive a reverse shock, low grain growth efficiencies ($\epsilon$ = 30–40), and long dust lifetimes (1–2 Gyr).

(ii) the contribution from stardust (>90 per cent) outweighs the fraction of dust grown through accretion in the ISM (<10 per cent) over the entire lifetime of these galaxies, while present-day dust budgets have similar contributions from stellar sources (50–80 per cent) and ISM dust growth (20–50 per cent).

(iii) the specific shape of the SFH does not strongly influence the model outcome due to these long dust lifetimes.

We demonstrate in this paper that local galaxy scaling relations can be accounted for by efficient supernova dust production, low grain growth efficiencies, and long dust lifetimes. We speculate that these models provide an alternative to earlier work that required vigorous dust destruction and efficient grain growth on time-scales of $\lesssim$ a few Myr (e.g. Draine 2009; Zhukovska 2014; Feldmann 2015; De Vis et al. 2017b) to explain local galaxy scaling relations. These long dust lifetimes and reduced grain growth efficiencies could reduce the tension with grain-surface chemical models (e.g. Barlow 1978; Ferrara et al. 2016; Ceccarelli et al. 2018; Jones & Ysard 2019) that have not been able to come up with efficient grain growth mechanisms in interstellar clouds. Our model results might furthermore help solving the dust budget problem at high redshifts (e.g. Bertoldi et al. 2003; Priddey et al. 2003; Watson et al. 2015), in case similar dust production and destruction efficiencies would apply to those primordial galaxies.

We caution that model parameter degeneracies between supernova dust production, grain growth, and dust destruction efficiencies cannot fully be resolved based on the current set of global galaxy scaling laws presented in this work. In future work, we plan to

Downloaded from https://academic.oup.com/mnras/article/496/3/3668/5850384 by University College London user on 24 September 2020

expand DEUS with radially dependent gaseous flows, to explore alternative recipes to describe grain growth and dust destruction processes, and to include additional observational constraints (e.g. resolved galaxy properties, and depletion factors for various elements).

## ACKNOWLEDGEMENTS

We would like to thank the anonymous referee for her/his suggestions that have improved the presentation of the fitting methods and results reported in this paper. IDL gratefully acknowledges the support of the Research Foundation – Flanders (FWO). LCH was supported by the National Science Foundation of China (11721303) and the National Key R&D Programme of China (2016YFA0400702). MJM acknowledges the support of the National Science Centre, Poland through the SONATA BIS grant 2018/30/E/ST9/00208.

The JCMT is operated by the East Asian Observatory on behalf of The National Astronomical Observatory of Japan, Academia Sinica Institute of Astronomy and Astrophysics, the Korea Astronomy and Space Science Institute, the National Astronomical Observatories of China, and the Chinese Academy of Sciences (Grant No. XDB09000000), with additional funding support from the Science and Technology Facilities Council of the United Kingdom and participating universities in the United Kingdom and Canada. Additional funds for the construction of SCUBA-2 were provided by the Canada Foundation for Innovation. These data are being observed under JCMT Project ID: M16AL005. The Starlink software (Currie et al. 2014) used as part of the JINGLE data reduction process is currently supported by the East Asian Observatory.

PACS was developed by a consortium of institutes led by MPE (Germany) and including UVIE (Austria); KU Leuven, CSL, IMEC (Belgium); CEA, LAM (France); MPIA (Germany); INAFIFSI/OAA/OAP/OAT, LENS, SISSA (Italy); and IAC (Spain). This development has been supported by the funding agencies BMVIT (Austria), ESA-PRODEX (Belgium), CEA/CNES (France), DLR (Germany), ASI/INAF (Italy), and CICYT/MCYT (Spain). SPIRE was developed by a consortium of institutes led by Cardiff University (UK) and including Univ. Lethbridge (Canada); NAOC (China); CEA, LAM (France); IFSI, Univ. Padua (Italy); IAC (Spain); Stockholm Observatory (Sweden); Imperial College London, RAL, UCL-MSSL, UKATC, Univ. Sussex (UK); and Caltech, JPL, NHSC, Univ. Colorado (USA). This development has been supported by national funding agencies: CSA (Canada); NAOC (China); CEA, CNES, CNRS (France); ASI (Italy); MCINN (Spain); SNSB (Sweden); STFC and UKSA (UK); and NASA (USA).

## REFERENCES

Accurso G. et al., 2017, MNRAS, 470, 4750
Amorín R., Muñoz-Tuñón C., Aguerri J. A. L., Planesas P., 2016, A&A, 588, A23
An D., 2019, ApJ, 878, L31
Aoyama S., Hou K.-C., Shimizu I., Hirashita H., Todoroki K., Choi J.-H., Nagamine K., 2017, MNRAS, 466, 105
Asano R. S., Takeuchi T. T., Hirashita H., Inoue A. K., 2013, Earth Planets Space, 65, 213
Asplund M., Grevesse N., Sauval A. J., Scott P., 2009, ARA&A, 47, 481
Aver E., Olive K. A., Porter R. L., Skillman E. D., 2013, J. Cosmol. Astropart. Phys., 11, 017
Balser D. S., 2006, AJ, 132, 2326
Barlow M. J., 1978, MNRAS, 183, 417
Barlow M. J. et al., 2010, A&A, 518, L138
Belfiore F. et al., 2017, MNRAS, 469, 151
Belfiore F., Vincenzo F., Maiolino R., Matteucci F., 2019, MNRAS, 487, 456
Bertoldi F., Carilli C. L., Cox P., Fan X., Strauss M. A., Beelen A., Omont A., Zylka R., 2003, A&A, 406, L55
Bevan A., Barlow M. J., 2016, MNRAS, 456, 1269
Bianchi S., Schneider R., 2007, MNRAS, 378, 973
Bianchi S. et al., 2018, A&A, 620, A112
Bigiel F., Leroy A., Walter F., Brinks E., de Blok W. J. G., Madore B., Thornley M. D., 2008, AJ, 136, 2846
Biscaro C., Cherchneff I., 2016, A&A, 589, A132
Bocchio M., Marassi S., Schneider R., Bianchi S., Limongi M., Chieffi A., 2016, A&A, 587, A157
Bolatto A. D., Wolfire M., Leroy A. K., 2013, ARA&A, 51, 207
Boselli A., Boissier S., Cortese L., Gil de Paz A., Seibert M., Madore B. F., Buat V., Martin D. C., 2006, ApJ, 651, 811
Boselli A. et al., 2010, PASP, 122, 261
Boselli A., Cortese L., Boquien M., 2014a, A&A, 564, A65
Boselli A., Cortese L., Boquien M., Boissier S., Catinella B., Lagos C., Saintonge A., 2014b, A&A, 564, A66
Bothwell M. S., Maiolino R., Kennicutt R., Cresci G., Mannucci F., Marconi A., Cicone C., 2013, MNRAS, 433, 1425
Boyer M. L. et al., 2019, ApJ, 879, 109
Bundy K. et al., 2015, ApJ, 798, 7
Calura F., Pipino A., Matteucci F., 2008, A&A, 479, 669
Carniani S. et al., 2017, A&A, 605, A42
Casasola V. et al., 2020, A&A, 633, A100
Catinella B. et al., 2018, MNRAS, 476, 875
Ceccarelli C., Viti S., Balucani N., Taquet V., 2018, MNRAS, 476, 1371
Chabrier G., 2003, PASP, 115, 763
Cicone C. et al., 2014, A&A, 562, A21
Ciesla L. et al., 2012, A&A, 543, A161
Ciesla L. et al., 2016, A&A, 585, A43
Cigan P. et al., 2019, ApJ, 886, 51
Clark C. J. R. et al., 2015, MNRAS, 452, 397
Clark C. J. R., Schofield S. P., Gomez H. L., Davies J. I., 2016, MNRAS, 459, 1646
Clark C. J. R. et al., 2018, A&A, 609, A37
Clark C. J. R. et al., 2019, MNRAS, 489, 5256
Cormier D. et al., 2015, A&A, 578, A53
Cormier D. et al., 2019, A&A, 626, A23
Cortese L., Catinella B., Boissier S., Boselli A., Heinis S., 2011, MNRAS, 415, 1797
Cortese L. et al., 2012, A&A, 540, A52
Cortese L. et al., 2014, MNRAS, 440, 942
Cortese L. et al., 2016, MNRAS, 459, 3574
Cowie L. L., Songaila A., Hu E. M., Cohen J. G., 1996, AJ, 112, 839
Currie M. J., et al., 2014, Astronomical Data Analysis Software and Systems XXIII. Proceedings, 485, 391
da Cunha E., Eminian C., Charlot S., Blaizot J., 2010, MNRAS, 403, 1894
Dale D. A., Helou G., Contursi A., Silbermann N. A., Kolhatkar S., 2001, ApJ, 549, 215
Dale D. A. et al., 2017, ApJ, 837, 90
De Cia A., Ledoux C., Mattsson L., Petitjean P., Srianand R., Gavignaud I., Jenkins E. B., 2016, A&A, 596, A97
De Looze I. et al., 2016, MNRAS, 459, 3900
De Looze I., Barlow M. J., Swinyard B. M., Rho J., Gomez H. L., Matsuura M., Wesson R., 2017a, MNRAS, 465, 3309
De Looze I. et al., 2017b, MNRAS, 465, 3741
De Looze I. et al., 2019, MNRAS, 488, 164
De Vis P. et al., 2017a, MNRAS, 464, 4680
De Vis P. et al., 2017b, MNRAS, 471, 1743
De Vis P. et al., 2019, A&A, 623, A5
Dekel A. et al., 2009, Nature, 457, 451
Dell'Agli F., Valiante R., Kamath D., Ventura P., García-Hernández D. A., 2019, MNRAS, 486, 4738
Demyk K. et al., 2017a, A&A, 600, A123
Demyk K. et al., 2017b, A&A, 606, A50

Downloaded from https://academic.oup.com/mnras/article/496/3/3668/5850384 by University College London user on 24 September 2020

Draine B. T., 2009, in Henning T., Grün E., Steinacker J., eds, ASP Conf. Ser. Vol. 414, Cosmic Dust - Near and Far. Astron. Soc. Pac., San Francisco, p. 453
Driver S. P., Popescu C. C., Tuffs R. J., Liske J., Graham A. W., Allen P. D., de Propris R., 2007, MNRAS, 379, 1022
Dwek E., 1998, ApJ, 501, 643
Eales S. et al., 2010, PASP, 122, 499
Eales S. et al., 2012, ApJ, 761, 168
Eales S., de Vis P., Smith M. W. L., Appah K., Ciesla L., Duffield C., Schofield S., 2017, MNRAS, 465, 3125
Feldmann R., 2015, MNRAS, 449, 3274
Ferrara A., Viti S., Ceccarelli C., 2016, MNRAS, 463, L112
Ferrarotti A. S., Gail H.-P., 2006, A&A, 447, 553
Fluetsch A. et al., 2019, MNRAS, 483, 4586
Foreman-Mackey D., Hogg D. W., Lang D., Goodman J., 2013, PASP, 125, 306
Galametz M., Madden S. C., Galliano F., Hony S., Bendo G. J., Sauvage M., 2011, A&A, 532, A56
Gall C. et al., 2014, Nature, 511, 326
Garnett D. R., 2002, ApJ, 581, 1019
Ginolfi M., Graziani L., Schneider R., Marassi S., Valiante R., Dell'Agli F., Ventura P., Hunt L. K., 2018, MNRAS, 473, 4538
Gomez H. L. et al., 2012, ApJ, 760, 96
Goodman J., Weare J., 2010, Commun. Appl. Math. Comput. Sci., 5, 65I
Graziani L., Schneider R., Ginolfi M., Hunt L. K., Maio U., Glatzle M., Ciardi B., 2019, MNRAS, 494, 1071
Groves B. A. et al., 2015, ApJ, 799, 96
Hartmann J., 1904, ApJ, 19, 286
Hashimoto T. et al., 2018, Nature, 557, 392
Haynes M. P., Giovanelli R., 1984, AJ, 89, 758
Haynes M. P. et al., 2018, ApJ, 861, 49
Hayward C. C., Hopkins P. F., 2017, MNRAS, 465, 1682
Henning T., Jäger C., Rouillé G., Fulvio D., Krasnokutski S. A., 2018, in Cunningham M., Millar T., Aikawa Y., eds, Proc. IAU Symp. 332, Astrochemistry VII: Through the Cosmos from Galaxies to Planets. Kluwer, Dordrecht, p. 312
Hirashita H., 2015, MNRAS, 447, 2937
Hughes T. M., Cortese L., Boselli A., Gavazzi G., Davies J. I., 2013, A&A, 550, A115
Hu C.-Y., Zhukovska S., Somerville R. S., Naab T., 2019, MNRAS, 487, 3252
Hunt L. K. et al., 2019, A&A, 621, A51
Hunter D. A., Zahedy F., Bowsher E. C., Wilcots E. M., Kepley A. A., Gaal V., 2011, AJ, 142, 173
Inoue A. K. et al., 2016, Science, 352, 1559
Janowiecki S., Cortese L., Catinella B., Goodwin A. J., 2018, MNRAS, 476, 1390
Jones A. P., Nuth J. A., 2011, A&A, 530, A44
Jones A. P., Ysard N., 2019, A&A, 627, A38
Jones A. P., Tielens A. G. G. M., Hollenbach D. J., McKee C. F., 1994, ApJ, 433, 797
Jones A. P., Tielens A. G. G. M., Hollenbach D. J., 1996, ApJ, 469, 740
Jones A. P., Fanciullo L., Köhler M., Verstraete L., Guillet V., Bocchio M., Ysard N., 2013, A&A, 558, A62
Jones A. P., Köhler M., Ysard N., Bocchio M., Verstraete L., 2017, A&A, 602, A46
Kalberla P. M. W., Kerp J., 2009, ARA&A, 47, 27
Kennicutt R. C., Jr, 1998, ApJ, 498, 541
Kennicutt R. C., Jr, Bresolin F., Garnett D. R., 2003, ApJ, 591, 801
Kennicutt R. C., Evans N. J., 2012, ARA&A, 50, 531
Kennicutt R. C. et al., 2011, PASP, 123, 1347
Kewley L. J., Ellison S. L., 2008, ApJ, 681, 1183
Kirchschlager F., Schmidt F. D., Barlow M. J., Fogerty E. L., Bevan A., Priestley F. D., 2019, MNRAS, 489, 4465
Kobulnicky H. A., Kewley L. J., 2004, ApJ, 617, 240
Köhler M., Jones A., Ysard N., 2014, A&A, 565, L9
Krasnokutski S. A., Rouillé G., Jäger C., Huisken F., Zhukovska S., Henning T., 2014, ApJ, 782, 15
Lakićević M. et al., 2015, ApJ, 799, 50
Lamperti I. et al., 2019, MNRAS, 489, 4389 (JINGLE Paper V)
Laporte N. et al., 2017, ApJ, 837, L21
Lebouteiller V. et al., 2012, A&A, 548, A91
Leroy A. K., Walter F., Brinks E., Bigiel F., de Blok W. J. G., Madore B., Thornley M. D., 2008, AJ, 136, 2782
Lian J., Thomas D., Maraston C., Goddard D., Comparat J., Gonzalez-Perez V., Ventura P., 2018a, MNRAS, 474, 1143
Lian J. et al., 2018b, MNRAS, 476, 3883
Lisenfeld U., Ferrara A., 1998, ApJ, 496, 145
Madden S. C., Cormier D., 2019, in McQuinn K. B. W., Stierwalt S., eds, Proc. IAU Symp. 344, Dwarf Galaxies: From the Deep Universe to the Present. Kluwer, Dordrecht, p. 240
Magdis G. E. et al., 2012, ApJ, 760, 6
Magrini L. et al., 2011, A&A, 535, A13
Mancini M., Schneider R., Graziani L., Valiante R., Dayal P., Maio U., Ciardi B., Hunt L. K., 2015, MNRAS, 451, L70
Marassi S., Schneider R., Limongi M., Chieffi A., Graziani L., Bianchi S., 2019, MNRAS, 484, 2587
Markwardt C. B., 2009, in Bohlender D. A., Durand D., Dowler P., eds, ASP Conf. Ser. Vol. 411, Astronomical Data Analysis Software and Systems XVIII. Astron. Soc. Pac., San Francisco, p. 251
Matsuura M., Woods P. M., Owen P. J., 2013, MNRAS, 429, 2527
Matsuura M. et al., 2015, ApJ, 800, 50
Matsuura M. et al., 2019, MNRAS, 482, 1715
Mattsson L., Andersen A. C., 2012, MNRAS, 423, 38
Mattsson L., Andersen A. C., Munkhammar J. D., 2012, MNRAS, 423, 26
McKee C., 1989, in Allamandola L. J., Tielens A. G. G. M., eds, Proc. IAU Symp. 135, Interstellar Dust. Kluwer, Dordrecht, p. 431
Mesa-Delgado A., Esteban C., García-Rojas J., Luridiana V., Bautista M., Rodríguez M., López-Martín L., Peimbert M., 2009, MNRAS, 395, 855
Micelotta E. R., Dwek E., Slavin J. D., 2016, A&A, 590, A65
Michałowski M. J., 2015, A&A, 577, A80
Michałowski M. J., Murphy E. J., Hjorth J., Watson D., Gall C., Dunlop J. S., 2010, A&A, 522, A15
Morgan H. L., Edmunds M. G., 2003, MNRAS, 343, 427
Moustakas J., Kennicutt R. C., Jr, Tremonti C. A., Dale D. A., Smith J.-D. T., Calzetti D., 2010, ApJS, 190, 233
Muratov A. L., Kereš D., Faucher-Giguère C.-A., Hopkins P. F., Quataert E., Murray N., 2015, MNRAS, 454, 2691
Naab T., Ostriker J. P., 2017, ARA&A, 55, 59
Nanni A., Bressan A., Marigo P., Girardi L., 2013, MNRAS, 434, 2390
Nath B. B., Laskar T., Shull J. M., 2008, ApJ, 682, 1055
Nersesian A. et al., 2019, A&A, 624, A80
Noeske K. G. et al., 2007, ApJ,dge 660, L43
Nozawa T., Kozasa T., Habe A., Dwek E., Umeda H., Tominaga N., Maeda K., Nomoto K., 2007, ApJ, 666, 955
Oldham L., Auger M., 2018, UK, MNRAS, 474, 4169
Pagel B. E. J., 1997, Nucleosynthesis and Chemical Evolution of Galaxies. Cambridge Univ. Press, Cambridge UK
Pannella M. et al., 2009, ApJ, 698, L116
Pappalardo C., Lançon A., Vollmer B., Ocvirk P., Boissier S., Boselli A., 2010, A&A, 514, A33
Peters T. et al., 2017, MNRAS, 467, 4322
Pettini M., Pagel B. E. J., 2004, MNRAS, 348, L59
Planck Collaboration XXIX, 2016, A&A, 586, A132
Poetrodjojo H. et al., 2018, MNRAS, 479, 5235
Popping G., Somerville R. S., Trager S. C., 2014, MNRAS, 442, 2398
Popping G., Somerville R. S., Galametz M., 2017, MNRAS, 471, 3152
Prantzos N., Casse M., Vangioni-Flam E., 1993, ApJ, 403, 630
Priddey R. S., Isaak K. G., McMahon R. G., Robson E. I., Pearson C. P., 2003, MNRAS, 344, L74
Priestley F. D., Barlow M. J., De Looze I., 2019, MNRAS, 485, 440
Priestley F. D., Barlow M. J., De Looze I., Chawner H., 2020, MNRAS, 491, 6020
Rémy-Ruyer A. et al., 2014, A&A, 563, A31
Rémy-Ruyer A. et al., 2015, A&A, 582, A121

Downloaded from https://academic.oup.com/mnras/article/496/3/3668/5850384 by University College London user on 24 September 2020

Robitaille T. P., Whitney B. A., 2010, ApJ, 710, L11
Rodighiero G. et al., 2010, A&A, 518, L25
Rouillé G., Jäger C., Krasnokutski S. A., Krebsz M., Henning T., 2014, Faraday Discussions, 168, 449
Rowlands K., Gomez H. L., Dunne L., Aragón-Salamanca A., Dye S., Maddox S., da Cunha E., van der Werf P., 2014, MNRAS, 441, 1040
Saintonge A. et al., 2011, MNRAS, 415, 32
Saintonge A. et al., 2016, MNRAS, 462, 1749
Saintonge A. et al., 2018, MNRAS, 481, 3497 (JINGLE Paper I)
Sánchez S. F. et al., 2017, MNRAS, 469, 2121
Sánchez Almeida J., Elmegreen B. G., Muñoz-Tuñón C., Elmegreen D. M., 2014, A&AR, 22, 71
Sánchez-Blázquez P. et al., 2014, A&A, 570, A6
Sandstrom K. M. et al., 2013, ApJ, 777, 5
Santini P. et al., 2017, ApJ, 847, 76
Sarangi A., Cherchneff I., 2015, A&A, 575, A95
Schaller G., Schaerer D., Meynet G., Maeder A., 1992, A&AS, 96, 269
Schmidt M., 1959, ApJ, 129, 243
Schneider R., Hunt L., Valiante R., 2016, MNRAS, 457, 1842
Schruba A. et al., 2012, AJ, 143, 138
Scoville N. et al., 2014, ApJ, 783, 84
Scoville N. et al., 2016, ApJ, 820, 83
Silk J., Mamon G. A., 2012, Res. Astron. Astrophys., 12, 917
Silvia D. W., Smith B. D., Shull J. M., 2010, ApJ, 715, 1575
Slavin J. D., Dwek E., Jones A. P., 2015, ApJ, 803, 7
Smit R. et al., 2014, ApJ, 784, 58
Smith M. W. L. et al., 2012, ApJ, 748, 123
Smith M. W. L. et al., 2019, MNRAS, 486, 4166 (JINGLE Paper II)
Temim T., Dwek E., 2013, ApJ, 774, 8
Temim T., Dwek E., Tchernyshyov K., Boyer M. L., Meixner M., Gall C., Roman-Duval J., 2015, ApJ, 799, 158
Temim T., Dwek E., Arendt R. G., Borkowski K. J., Reynolds S. P., Slane P., Gelfand J. D., Raymond J. C., 2017, ApJ, 836, 129
Thomas D. et al., 2013, MNRAS, 431, 1383
Tremonti C. A. et al., 2004, ApJ, 613, 898
Triani D. P., Sinha M., Croton D. J., Pacifici C., Dwek E., 2020, MNRAS, 493, 2490
Trumpler R. J., 1930, PASP, 42, 214
Valiante R., Schneider R., Bianchi S., Andersen A. C., 2009, MNRAS, 397, 1661
Valiante R., Schneider R., Salvadori S., Bianchi S., 2011, MNRAS, 416, 1916
van den Hoek L. B., Groenewegen M. A. T., 1997, A&AS, 123, 305
Vílchez J. M., Relaño M., Kennicutt R., De Looze I., Mollá M., Galametz M., 2019, MNRAS, 483, 4968
Walter F. et al., 2017, ApJ, 835, 265
Watson D., Christensen L., Knudsen K. K., Richard J., Gallazzi A., Michałowski M. J., 2015, Nature, 519, 327
Wesson R., Barlow M. J., Matsuura M., Ercolano B., 2015, MNRAS, 446, 2089
Woosley S. E., Weaver T. A., 1995, ApJS, 101, 181
Zapartas E. et al., 2017, A&A, 601, A29
Zhukovska S., 2014, A&A, 562, A76
Zhukovska S., Dobbs C., Jenkins E. B., Klessen R. S., 2016, ApJ, 831, 147
Zhukovska S., Henning T., Dobbs C., 2018, ApJ, 857, 94

## SUPPORTING INFORMATION

Supplementary data are available at *MNRAS* online.

**JINGLEIV_paper_Appendix_final.pdf**

Please note: Oxford University Press is not responsible for the content or functionality of any supporting materials supplied by the authors. Any queries (other than missing material) should be directed to the corresponding author for the article.

[1] *Sterrenkundig Observatorium, Ghent University, Krijgslaan 281 – S9, B-9000 Ghent, Belgium*
[2] *Department of Physics & Astronomy, University College London, Gower Street, London WC1E 6BT, UK*
[3] *Departamento Física Teórica y del Cosmos, Universidad de Granada, E-18071 Granada, Spain*
[4] *Instituto Universitario Carlos I de Física Teórica y Computacional, Universidad de Granada, E-18071 Granada, Spain*
[5] *School of Physics and Astronomy, Cardiff University, Queens Buildings, The Parade, Cardiff CF24 3AA, UK*
[6] *Space Telescope Science Institute, 3700 San Martin Drive, Baltimore, MD 21211, USA*
[7] *Department of Physics & Astronomy, McMaster University, Hamilton, ON L8S 4M1, Canada*
[8] *Institut d'Astrophysique Spatiale, Université Paris-Saclay, CNRS, F-91405 Orsay, France*
[9] *Steward Observatory, University of Arizona, 933 N Cherry Avenue, Tucson, AZ 85721-0065, USA*
[10] *George P. and Cynthia Woods Mitchell Institute for Fundamental Physics and Astronomy, Texas A&M University, College Station, TX 77843-4242, USA*
[11] *Centre for Astrophysics Research, University of Hertfordshire, College Lane, Hatfield AL10 9AB, UK*
[12] *Sub-department of Astrophysics, University of Oxford, Denys Wilkinson Building, Keble Road, Oxford OX1 3RH, UK*
[13] *Yonsei Frontier Lab and Department of Astronomy, Yonsei University, 50 Yonsei-ro, Seodaemun-gu, Seoul 03722, Republic of Korea*
[14] *Blackett Laboratory, Physics Department, Imperial College, London SW7 2AZ, UK*
[15] *Institute of Astronomy & Astrophysics, Academia Sinica, Taipei 10617, Taiwan*
[16] *Shanghai Astronomical Observatory, 80 Nandan Road, Xuhui District, Shanghai 200030, China*
[17] *Purple Mountain Observatory and Key Laboratory of Radio Astronomy, Chinese Academy of Sciences, Nanjing 210034, China*
[18] *Centre for Astronomy, National University of Ireland, University Road, Galway H91 TK33, Ireland*
[19] *Kavli Institute for Astronomy and Astrophysics, Peking University, Beijing 100871, China*
[20] *Department of Astronomy, School of Physics, Peking University, Beijing 100871, China*
[21] *Korea Astronomy and Space Science Institute, 776 Daedeokdae-ro, Yuseong-gu, Daejeon 34055, Republic of Korea*
[22] *Astronomical Observatory Institute, Faculty of Physics, Adam Mickiewicz University, ul. Słoneczna 36, PL-60-286 Poznań, Poland*
[23] *Tsinghua Center for Astrophysics and Physics Department, Tsinghua University, Beijing 100084, China*
[24] *Shanghai Astronomical Observatory, Chinese Academy of Sciences, 80 Nandan Road, Shanghai 200030, China*
[25] *Max Planck Institute for Astronomy, Königstuhl 17, D-69117 Heidelberg, Germany*
[26] *Astronomy Centre, Department of Physics and Astronomy, University of Sussex, Brighton BN1 9QH, UK*
[27] *Department of Physics, Zhejiang University, Hangzhou, Zhejiang 310027, China*
[28] *National Astronomical Observatory of China, 20A Datun Road, Chaoyang District, Beijing 100012, China*

This paper has been typeset from a TEX/LATEX file prepared by the author.

Downloaded from https://academic.oup.com/mnras/article/496/3/3668/5850384 by University College London user on 24 September 2020